MEASUREMENT OF THE VORTEX DEPINNING FORCE IN A HIGH TEMPERATURE SUPERCONDUCTOR

by

ANDREW PATRICK WHITEHEAD

Submitted to the Department of Physics in partial fulfillment of the Requirements for the Degree of

BACHELOR OF SCIENCE

at the

MASSACHUSETTS INSTITUTE OF TECHNOLOGY

June, 2005

Signature of Author _____
Department of Physics
May 4th, 2005

Certified by _____
Professor Eric Hudson
Department of Physics

Accepted by _____
Professor David E. Pritchard
Senior Thesis Coordinator, Department of Physics

Measurement of the Vortex Depinning Force in a High Temperature Superconductor

Andrew Whitehead

Physics Department

MIT, 77 Massachusetts Ave.

Cambridge, MA 02139-4307

Contents

List of Figures

1 Introduction

Superconductivity is one of those subjects in physics that is as captivating theoretically as it is experimentally interesting. The dual driving force of commercial demand for high-temperature superconductors (HTSC's), coupled with the intense basic science interest in uncovering the elusive mechanism that explains high temperature superconductivity has led to some ten thousand publications since the discovery of $LaBaCuO_4$ in 1986 [2]. Yet despite much progress in theory, material development and experimental techniques and measurement, many questions still remained unanswered.

Much of the difficulty in studying the properties of HTSC's arises from the inhomogeneity of their superconducting behavior, which arises from physical and electronic structure effects. Bulk measurements of the fundamental quantities yield limited information about the underlying mechanism because such measurements are averages of locally varying properties. For example, bulk vortex depinning measurements reveal little about how individual vortices pin within a superconductor.

In this thesis I will describe my attempt to get around the problems of bulk measurements by using a local probe technique known as Magnetic Force Microscopy (MFM) to make local magnetic field measurements. MFM is based on atomic force microscopy (AFM). The atomic force microscope was invented in 1986 [12] and its initial publication ranks as one of the top 5 cited references in all of *Physical Review Letters* [3]. Cantilever based measurement systems, including those that make magnetic measurements, are now commonplace for room temperature surface studies. Low temperature systems focusing on magnetism remain rare however.

This thesis presents an easily repeatable MFM measurement technique that can be used to extract the a great deal of information from individual vortices in YBCO. The intent is to use this same technique in the future to study the same quantity in many different materials, such that the quantitative results can be compared.

The device used in this experiment was constructed by Dr. Eric Straver, a graduate of Stanford University under the direction of Prof. Kathryn Moler. For his thesis, Eric constructed a magnetic force microscope, and used it to carry out depinning probability measurements on niobium and YBCO.

Using this device, Prof. Jenny Hoffman of Harvard University and I have developed a method of fully characterizing individual vortices. An individual measurement using this technique provides a full set of curves at different tip-sample distances de-

scribing force exerted on a vortex by the magnetic tip. As each scan of the MFM tip exerts an increasing lateral force on the vortex, should a given scan depin a vortex, it is possible to extract the force that was required to depin that particular vortex.

The results of thesis provide motivation for further use of this technique. The results we present were done using YBCO near its transition temperature, T_c, but this experiment can easily be extended to other temperatures, magnetic fields, and materials.

The organization of this thesis is as follows. Chapter two introduces the basic physics of superconductors with a focus on theory relevant to the work done in this paper, as well as a brief overview of current research as motivation for this experiment. Chapter three introduces the basics of cantilever measurements, as well as the technique of frequency modulation that is used to make these measurements. Chapter four describes the MFM apparatus and signal detection. Chapter five explains the method of scanning and shows sample data. Chapter six explains modelling that was used for real as well as idealized data. Finally, I will calculate the depinning force of a single vortex. In conclusion, I will motivate how this experiment can be continued and expanded to solve further problems in modern superconductor physics.

2 Basic Physics of Superconductivity

2.1 Unperturbed Superconductors

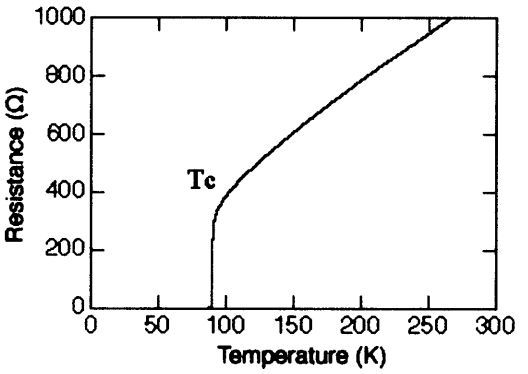

Figure 1: A sample plot of resistance vs. temperature for a HTSC. The critical T_c is shown where the resistance of the superconductor drops to zero.

Superconductivity was discovered in 1911 by Kamerlingh Onnes [13], several years after the first liquefaction of helium. Onnes found that resistance dropped to zero in samples of Mercury as temperature dropped below 4 K. A sample plot of such an experiment done in YBCO is shown in figure (1). That is, that electrons flowing through a superconductor experienced no resistance to flow through the material. The two-fluid model is an early description of superconductivity which proposed that electrons could be divided into two different categories: superconducting electrons and normal electrons. Even though only a small fraction of the total electrons may be superconducting, this fraction is enough to "short" the material and cause the resistance to drop to zero. Though simplistic, this categorization of electrons serves useful even in more complex theories.

In 1950 the Ginzburg-Landau (GL) theory of superconductivity was published [17]. It introduces a pseudo-wavefunction ψ, which describes the motion superconducting electrons, where n_s is the density of superconducting electrons in the material such that $n_s = |\psi(x)|^2$. The mysterious thing about GL theory was that electrons, which are fermions, were said to have one total wavefunction describing their behavior. This seemed at odds with the Pauli exclusion principle, which places restrictions on how many electrons may have the same energy and wavefunction.

In 1957 Bardeen, Cooper, and Schrieffer (BCS) put forth a ground breaking micro-

scopic description of superconductivity that incorporated all previous theories, and explained recent developments [16]. The essence of BCS theory is that electrons in a superconductor pair via a weak attractive interaction due to phonons (lattice vibrations) that exist naturally in the crystal lattice. Since electrons are fermions, when they pair they form bosons, which are not restricted by the Pauli exclusion principle, and can thus all condense into the same energy state. The distance between individual electrons in each pair is denoted the coherence length, ξ_0, and is a material dependent property of superconductors.

The details of theory state that this condensation occurs because the fermi surface of electrons is unstable to attractive forces, such as phonon coupling. BCS puts requirements on pairing, such that pairs of electrons must be of opposite spin and momentum, thus when a pair scatters, momentum is always conserved. This way, these electron pairs, known as Cooper Pairs, can move cooperatively through a crystal without losing forward momentum, and hence superconductivity [16][2]. Earlier electrons were divided into two categories based on whether they were superconducting or not. Here we see that the difference between the two types of electrons is that superconducting electrons are simply paired electrons, whereas normal electrons are not.

BCS was the first quantum mechanical description of superconductivity. While it allows a complete description of superconductivity from the point of view of individual particle interactions, it is complicated and difficult to use.

2.2 Superconductors in a Magnetic Field

The second major property of superconductors is that they abhor having any internal magnetic field. This was discovered by Meissner and Ochsenfeld in 1933, and is known as the Meissner effect [14]. If a superconductor is put in an external magnetic field, a current will flow along its surface to counteract and prevent any internal magnetic field, shown in figure (2).

The onset of superconductivity is a temperature dependent effect. In initial tests done on the first few superconducting materials, the onset of superconducting was a sudden event occurring at a temperature distinct to each material, known as the critical temperature T_c. Furthermore, while superconducting these materials expelled external magnetic fields up to a certain critical field, H_c, where if the field exceeded H_c, superconductivity was quenched.

The London theory of superconductivity was the first to describe the Meissner

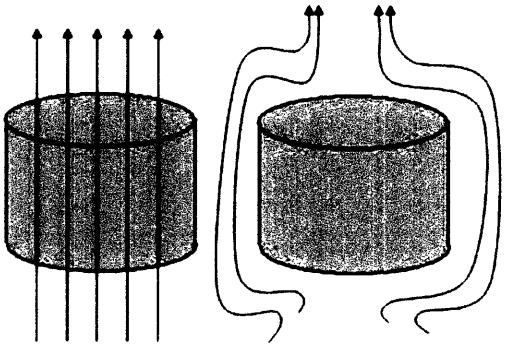

Figure 2: On the left, a material in a uniform magnetic field with $T > T_c$, and on the right, the material cooled such that $T < T_c$ illustrating the Meissner effect.

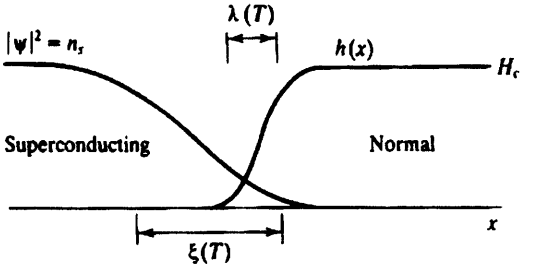

Figure 3: Picture illustrating the penetration depth λ and the coherence length ξ. It shows the density of superconducting electrons falling off as the edge of the superconductor approaches, along with an increase of magnetic field penetration as the non-superconducting regime is entered [7].

effect. London theory states that a magnetic field impinging on a superconductor is screened exponentially over a characteristic length scale λ known as the penetration depth. This is shown in figure (3). In order to screen magnetic field, a surface current of superconducting electrons flows to counteract external fields.

Despite development of modern quantum mechanical descriptions of superconductivity, the London theory is still used as a starting point for many experimental observations. Since the penetration depth is different in every material, its measurement provides information about other related properties of superconductors that are relevant in the study of new superconductors.

2.3 Type I and Type II Superconductivity

In the first discovered superconductors, the ratio of the penetration depth to the coherence length $\kappa = \lambda/\xi$ was always small. This means that in order to bring a magnetic field into a material past a distance λ, a much larger region ξ must be turned from superconducting to normal. In 1957, Abrikosov postulated what would happen if κ were large instead [18]. In this case one could allow magnetic fields to penetrate over a large region λ while only destroying superconductivity on a small scale ξ.

Materials of the appropriate value of κ, $\kappa > 1/\sqrt{2}$ according to Abrikosov, exhibit this behavior and are known as type II superconductors. Type II materials will transition to and from superconductivity more slowly through a range of magnetic fields, in contrast to the quick transition of traditional Type I materials through H_c. Experiments between the 1930's and 1950's verified this hypothesis.

In type II materials, since superconductivity is destroyed in small quantities, magnetic field penetration through a material also occurs in small quantities. Abrikosov used energy minimization and quantum mechanics arguments to come to the conclusion that magnetic field will penetrate a type II superconductor in a regular array of magnetic flux tubes.

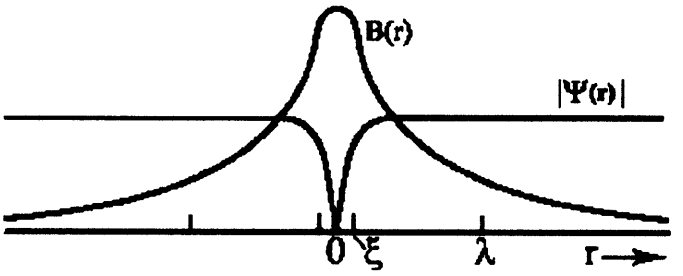

Figure 4: This plot of a vortex centered at the origin. It overlays the magnetic field penetrating the superconductor and density of superconducting electrons as a function of position [7].

Each flux tube, called a vortex, contains a normal core of electrons where the magnetic field penetrates and superconductivity is destroyed, as shown in figure (4). The area surrounding the vortices is superconducting and no magnetic field passes through. Quantum mechanics dictates that each vortex must contain exactly the same amount of magnetic flux Φ_0 where $\Phi_0 = hc/2e = 20.7$ Gauss μm^2. This differs

from the ordinary quanta of magnetic flux by a factor of two, because electrons are in a superconductor are paired.

The presence of vortices explains the gradual transition of superconducting materials. As the material is subjected to changing magnetic fields, superconductivity gradually changes a function of the number of vortices induced in the material.

2.4 Vortex Pinning

The vortex lattice suggested by Abrikosov has been successfully imaged by scanning tunnelling microscopy [20] as shown in figure (5). While in an ideal material vortex spacing would be equal, real materials have crystal inhomogeneities that lead to varying amounts of superconductivity and hence varying penalties that must be paid to create a vortex.

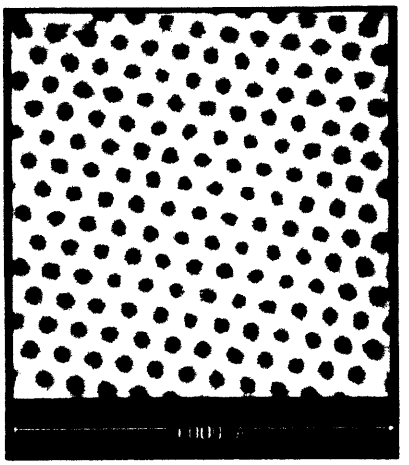

Figure 5: Abrikosov flux lattice in $NbSe_2$ imaged by STM. [20]

The presence of both normal and superconducting domains brings into question whether perfect conductivity still holds in the mixed state. Under an induced current, vortices feel a Lorentz force per unit length [7],

$$f_{lorentz} = \mathbf{J} \times \Phi_0 \tag{1}$$

tending to move them perpendicular to the direction of the current. This vortex motion is a dissipative force and leads to the destruction of superconductivity. In an ideal material, vortices should resist motion by a factor $\sim BR_{norm}/H_{c2}$ where

R_{norm} is the resistance of the normal state [7]. In real materials, inhomogeneities can serve as pinning sites for vortices against the Lorentz force. Under low to moderate currents, vortices will entirely resist motion, and superconductivity will remain. Figure (6) shows an example of such an inhomogeneity in YBCO. If the Lorentz force, however, exceeds the strength of the pinning site, then the vortices will move and superconductivity will be lost.

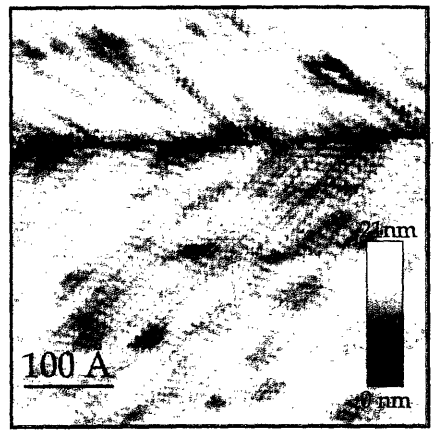

Figure 6: Image of a Twin Boundary in the CuO plane of YBCO. Figure from [4].

The questions of what causes pinning and how strong pinning forces are are central to the aim and motivation of the experiment. Understanding pinning is crucial to the application of superconductors with high currents and in high fields. It is also a fascinating basic physics question.

2.5 High Temperature Superconductivity

Following GL and BCS theory, superconductivity research reached a standstill. Theorists had predicted that a T_c of about 30 K was as high as could be expected given BCS theory, and there already existed several technologically useful materials that existed near that temperature. This complacency ended with the discovery of $LaBaCu0_4$ in 1986 [10], at a $T_c = 34$ K. A year later YBCO [11] was discovered with $T_c = 94$ K. This represented a major breakthrough as YBCO's T_c was above the liquefaction temperature of liquid Nitrogen at 77 K. Since that point superconductivity has experienced a resurgence that continues today. A graph showing the discovery year and T_c of many HTSC's is shown in figure (7).

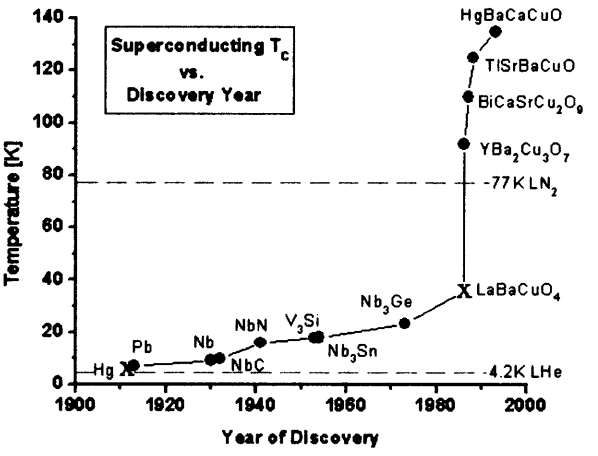

Figure 7: T_c discovery history, figure from [2]. "X" marks in red denote discoveries awarded Nobel prizes.

The crystal structure of all HTSCs are similar, with CuO_2 planes lying perpendicular to the c axis separated by other "dopant" layers. As a result all these materials are known as "cuprates". The crystal structure of YBCO is shown in figure (8) as an example. CuO_2 planes in these materials contain mobile charge carriers and are thought to be superconducting cooper pairs [8]. All cuprates are type II superconductors, but characteristic values of parameters such as λ and ξ are significantly different than in traditional type II materials. This results in several important effects [8]:

1. Cuprates have low carrier density. This leads to lower screening compared to normal metals, resulting in a larger average λ. In the CuO_2 plane of YBCO $\lambda = .2\mu$m compared with Niobium, an elemental type-II superconductor, where $\lambda = .09\mu$m.

2. Cuprates have extremely short coherence length ξ, where ξ_c can be as small as 0.3 nm, and $\xi_{ab} = 2$ nm. Short coherence length means cooper pairs coordinate motion over a much smaller distance. This makes them more vulnerable to break up due to thermal fluctuations, as well as topographic barriers such as impurities, and grain boundaries. This is in contrast to more moderate type II superconductors, where small ratios of κ make cooper pairs more resilient to surface and thermal effects.

3. Cuprates are highly anisotropic and very sensitive to local doping. Many are

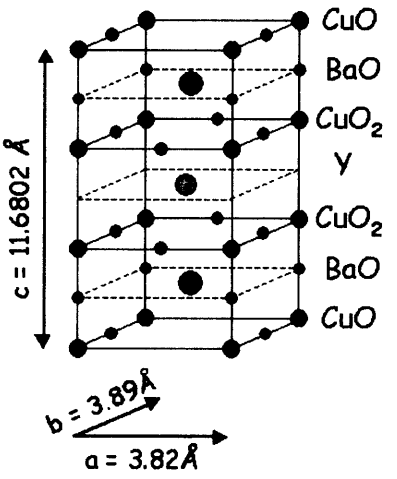

Figure 8: Crystal structure of YBCO.

only superconducting only in specific, non-stoichiometric compositions, and even then only in certain regions where doping is favorable.

When HTSC's first appeared, all the experiments that had been performed on conventional superconductors were repeated. A theory like BCS for HTSC's has not come forth, due at least partially to the often contradictory results that have arisen from such experiments.

The introduction of doping as a tunable parameter is the source of much experimentation in the search for a mechanism for high-temperature superconductivity. Since cuprates without doping are typically antiferromagnetic insulators, and since conventional wisdom says superconductivity cannot coexist with magnetism [2], the phase space of cuprates is a common source of study because in these highly anisotropic materials, it is often possible to see both of these occurring simultaneously in samples under study. Doping, along with temperature and applied magnetic field, together provide three different ways in which to design and affect superconducting behavior. Figure (9) shows behavior of superconductivity as a function of these parameters. The proof of a mechanism for high temperature superconductivity becomes as much a materials science question as it does a physics question, as developing materials in some regions of the phase space is as difficult an engineering task as measuring its properties.

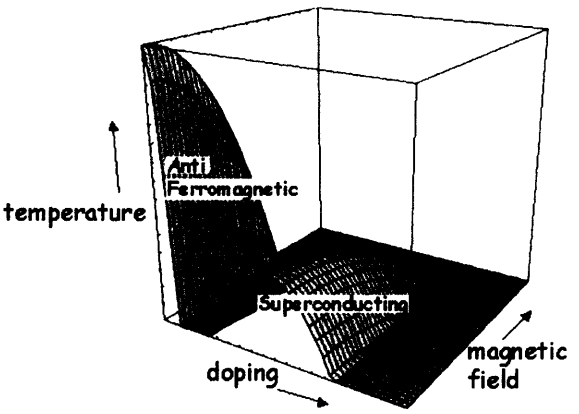

Figure 9: Phase diagram for high temperature superconductivity from [2]. While this phase space has been extensively studied and much is known about the antiferromagnetic and superconducting regimes, little is actually understood about their behavior and interaction.

2.6 Pinning Motivation and Current Research

Current applications of superconductivity make use of both primary properties of superconductivity, zero resistivity and flux exclusion, to operate. Yet, there are several limiting factors that continue to hinder the growth of the superconductor industry.

First, cooling has always made superconductivity a high cost technology. The invention of the cuprates has brought down the cost of cooling considerably, since liquid nitrogen can be used in place of liquid helium. Regardless, constant cooling and the apparatus to maintain it will continue to be a hindering aspect of the implementation of superconductors.

Though HTSC's are slowly solving this cooling problem, using cuprates in place of traditional superconductors brings to the forefront news problem in superconductor applications. From a production standpoint, cuprates are ceramics, thus it is very difficult to make wires out of them. Cuprates also have a limit to the amount of current they can carry before they cease to superconduct. Thus for superconductors to become more practically useful, not only must cooling requirements decrease, current capacities must improve as well. Since current capacity is directly correlated to vortex pinning strength, vortex pinning is an essential characteristic of superconductivity that requires more study.

Much effort has been put towards the study of pinning of vortices, but primarily from a bulk-flow point of view. Macroscopic scale currents are applied, resulting in

resistance measurements. While such experiments are useful characterizations, only microscopic scale studies can reveal the nature of pinning.

MFM in particular is an important tool for this kind of study because in MFM the tip interacts with the sample and exerts a force on it. Other local measurement tools, such as Hall Probes and SQUIDs, give local information but don't interact with the sample. Several groups have already taken advantage of this ability.

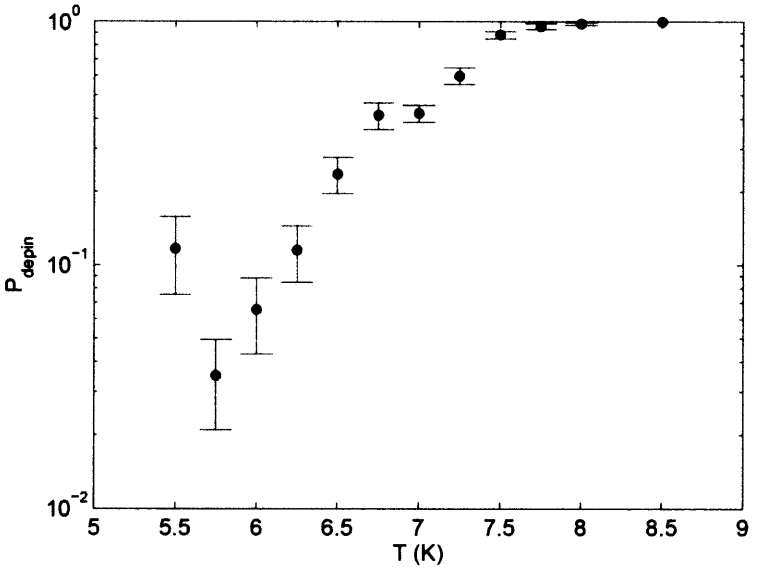

Figure 10: Probability of vortex depinning as a function of temperature in Niobium at a scan height of 90 nm. Figure from [1].

Eric Straver of Stanford University, who built the apparatus for this experiment, collected statistics on vortex depinning probability in Niobium as a function of temperature [1]. His results, shown in figure (10), support the hypothesis that vortices can depin by thermal activation, though it is currently not possible to tell whether this is due to increased energy at higher temperatures, or whether it is because the shape and size of the pinning potential well changes a function of temperature.

This temperature dependence is important because it suggests a course of action for future pinning research. For any vortex depinning research to be useful, a large data set is necessary to average out thermal effects. For instance, to find the pinning strength of various types of surface effects, the more measurements taken the better the average result will become.

Roseman and Grütter of McGill University are pursuing a new avenue of vortex

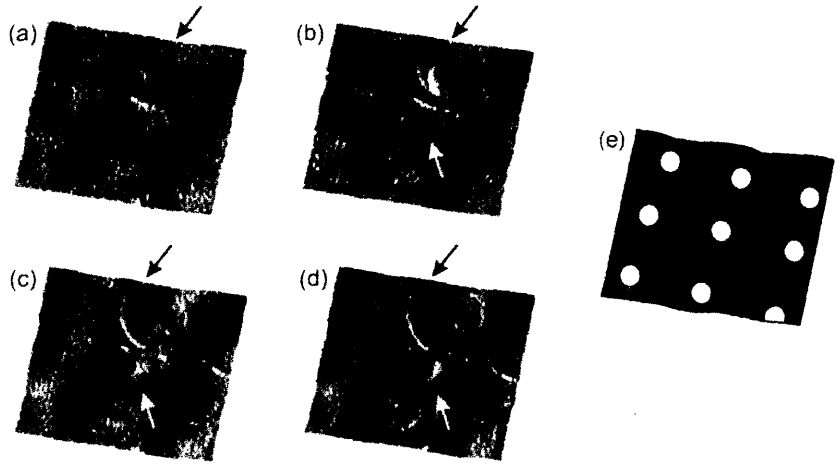

Figure 11: Figures (a) - (d) are constant height images taken by MFM of a patterned film of Nb. Interactions between the tip and the sample caused movement of the vortices within the antidots, as indicated by the arrows. Figure (e) is a cartoon showing the location of the antidots in the scan region. Figure taken from [24].

depinning measurements that represent a possible future direction for the technique developed in this thesis [24]. They have used laser interferometric lithography to create a lattice of antidots on a Niobium film substrate. The antidots act as artificial pinning sites for vortices. Remember the number of vortices in a materials increases linearly with increasing magnetic field. Thus in order to "fill" the antidots with vortices, a matching field must be found for the modified thin film in order to get the correct density of vortices such as to align with the antidot lattice. Results of their studies with antidot lattices are shown in figure (10).

Artificial pinning sites are the next step towards more efficient superconductor technology. By finding out what causes the strongest pinning sites, and how to create and arrange them in the crystal, material manufacturers could create higher current capacity superconductors.

Another interesting feature of their research is the correlated surface topography image they obtained via AFM, which corresponds to the same scan area as the MFM magnetic topography signal. Correlating AFM and MFM images allows researchers to map vortex pinning sites to surface properties. This will allow pinpointing of the mechanism for vortex pinning, and the ability to attribute vortex formation to specific effects like grain boundaries, twin boundaries, etc, rather than trying to select for samples believed to exhibit certain pinning-friendly characteristics.

3 Magnetic Force Microscopy

Magnetic Force Microscopy is a powerful tool for magnetic characterization. Its basic principle is simple, but obtaining quantitative information from data requires information about both the tip and well as the sample, and thus extracting data from an MFM experiment is a complex process. This section introduces cantilever principles, the Frequency Modulation (FM) detection method [21] used to take data in this experiment.

3.1 Cantilever Basics

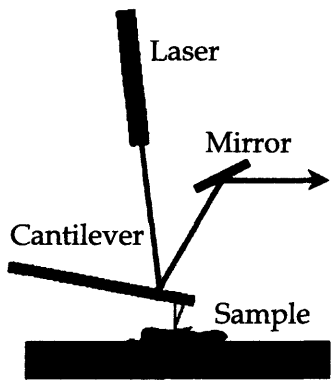

Figure 12: The basic setup of an AFM.

In atomic force microscopy (AFM) measurements, a small tip at the end of a cantilever interacts with a sample. A simple setup for AFM is shown in figure (12). A force exerted on the tip by the sample causes the cantilever to deflect. The cantilever can easily be modelled by a spring obeying Hooke's law,

$$F_{ts} = k(z - z_0) \tag{2}$$

where z_0 is the equilibrium cantilever displacement and F_{ts} is the force between the tip and the sample. Experimentally, this is accomplished by dragging the tip across the sample and measuring deflection. If the goal is to generate a picture of surface topography via atomic force microscopy, a variety of materials can be used to make the tip and the cantilever can be brought to rest on the surface. In the case of MFM, to obtain a picture of the sample's magnetic topography, the cantilever tip is coated

with a small amount of magnetic material at the end, and is dragged over the sample at the desired height to obtain an image. Typically this height is between 100 nm and a few micrometers.

Deflection is commonly measured in one of two ways. By far the most common method, and the one used in this experiment, is to use an interferometer to measure the path length change of a laser bounced off the back of the cantilever. It is also possible to use a piezoresistive cantilever, which incorporates a detection sensor into the cantilever itself, but these are more rare, have limited range of response and applicability, and typically have a lower signal to noise ratio [22],[21].

The cantilever can also be used to measure force gradients. This derivation follows from [1], which is derived from [6] and [3]. By driving the cantilever with a sinusoidal force, $F_d(t)$, the cantilever follows the equation of motion for a damped simple harmonic oscillator,

$$m\frac{d^2z}{dt^2} + \gamma\frac{dz}{dt} + k(z - z_0) = F_d(t) + F_{ts}(z) \tag{3}$$

where m is the mass of the cantilever and γ is the damping coefficient. In general, the tip-sample force $F_{ts}(z)$ acts over the whole cantilever, but experimental cantilevers are designed to minimize the force due to most of the cantilever, and maximize the influence of the tip. In MFM this is accomplished by adding magnetized material only to the tip, and not the cantilever. Taylor expanding the $F_{ts}(z)$ contribution, assuming small deflection the expression changes to:

$$m\frac{d^2z}{dt^2} + \gamma\frac{dz}{dt} + k(z - z_0) = F_d(t) + F_{ts}(z_0) + \frac{dF_{ts}}{dz}\,|_{z_0}\,(z - z_0) \tag{4}$$

It is useful to rearrange this equation and define an effective spring constant k_{eff}.

$$m\frac{d^2z}{dt^2} + \gamma\frac{dz}{dt} + (k - \frac{dF_{ts}}{dz}\,|_{z_0})(z - z_0) = F_d(t) + F_{ts}(z_0) \tag{5}$$

$$m\frac{d^2z}{dt^2} + \gamma\frac{dz}{dt} + k_{eff}(z - z_0) = F_d(t) + F_{ts}(z_0) \tag{6}$$

To measure force gradient, measure the shift in the cantilever's resonant frequency away from the driving frequency, $\Delta\omega$. In the presence and absence of a force gradient, the resonant frequency is given by ω_0' and ω_0, respectively:

$$\omega_0' = \sqrt{\frac{k_{eff}}{m}} \qquad \omega_0 = \sqrt{\frac{k}{m}} \tag{7}$$

The shift due to the force gradient is defined as $\Delta\omega = \omega_0' - \omega_0$. Taylor expanding k_{eff}, assuming the force gradient is much smaller than the spring constant, the expression for the frequency shift becomes:

$$\frac{\Delta\omega}{\omega_0} = -\frac{1}{2k}\frac{dF_{ts}}{dz}. \tag{8}$$

Using this equation, the force gradient can be measured by obtaining the frequency shift of cantilever away from its resonant frequency.

3.2 Frequency Modulation

The frequency modulation (FM) technique was developed in order to provide a higher sensitivity replacement to the conventional technique of cantilever measurement, "slope detection" [21]. FM detection works by measuring the frequency shift of the cantilever as data, then feeding back to drive the cantilever on that new resonant frequency to maintain a constant phase shift δ on the cantilever. A basic setup for an AFM microscope using FM detection is shown in figure (13).

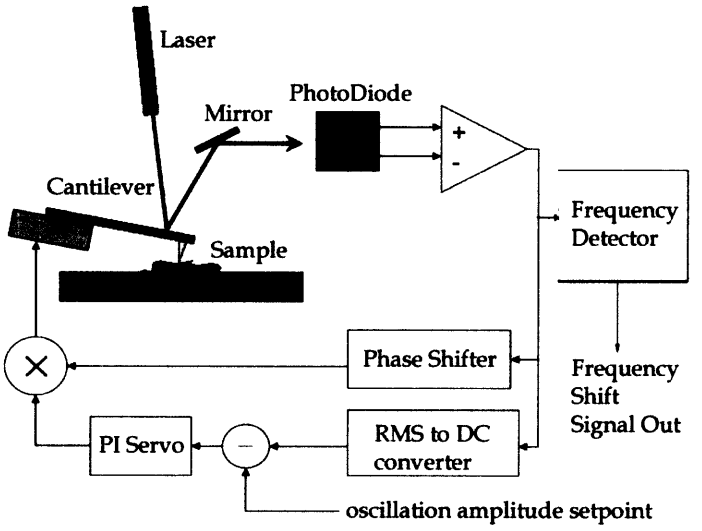

Figure 13: The setup of an AFM using FM detection. The photodiode measures the cantilever interferometer signal. The phase and amplitude control systems use positive feedback to maintain the resonant frequency. The PI servo amplifies voltages for input to the cantilever piezo. Figure from [3].

When a driven cantilever interacts with a force gradient, the response affects both the frequency of the cantilever (as shown in the section above), as well as the Q of

the cantilever. Changes in Q are due to energy dissipation through the interaction of the tip and the sample [1]. In FM one drives the cantilever at its resonant frequency but with a phase shift of $\pi/2$. At this frequency and phase shift, changes in Q due to dissipation have no effect on the feedback frequency [1]. This means that all of the information in the force gradient is measured by the frequency shift of the cantilever. In contrast, a method like "slope detection" loses some information to dissipation by driving the cantilever slightly off resonance.

This dissipation effect magnifies with increasing Q. Continuing with the example of the damped driven harmonic oscillator above, denote the driving force

$$F_d(t) = F_0 cos(\omega_d t) \tag{9}$$

and redefine the damping factor γ in terms of the quality factor Q of the cantilever,

$$\gamma = \frac{m\omega_0}{Q}. \tag{10}$$

Then the steady state motion of the cantilever in the absence of a force gradient is

$$z(t) = A_0 cos(\omega_d t + \delta_0), \tag{11}$$

and the solutions for the equilibrium values amplitude and phase shift values, A_0 and δ_0 respectively are:

$$A_0 = \frac{F_0/m}{(\omega_0^2 - \omega_d^2)^2 + (\omega_0\omega_d/Q)^2} \tag{12}$$

$$\delta_0 = \tan^{-1}\left[\frac{\omega_0\omega_d}{Q(\omega_0^2 - \omega_d^2)}\right]. \tag{13}$$

Looking at equation (13), maximizing the Q of the cantilever also maximizes the signal to noise ratio of a force gradient signal. Through proper cantilever design and the reduction of air damping in vacuum, it is possible to obtain very high Q values. In this experiment, our cantilever Q is approximately 160,000.

Figure (14) shows the amplitude A and the phase shift δ of a cantilever under the influence of two different force gradients. Notice that δ remains the same while the location of the peak of A shifts.

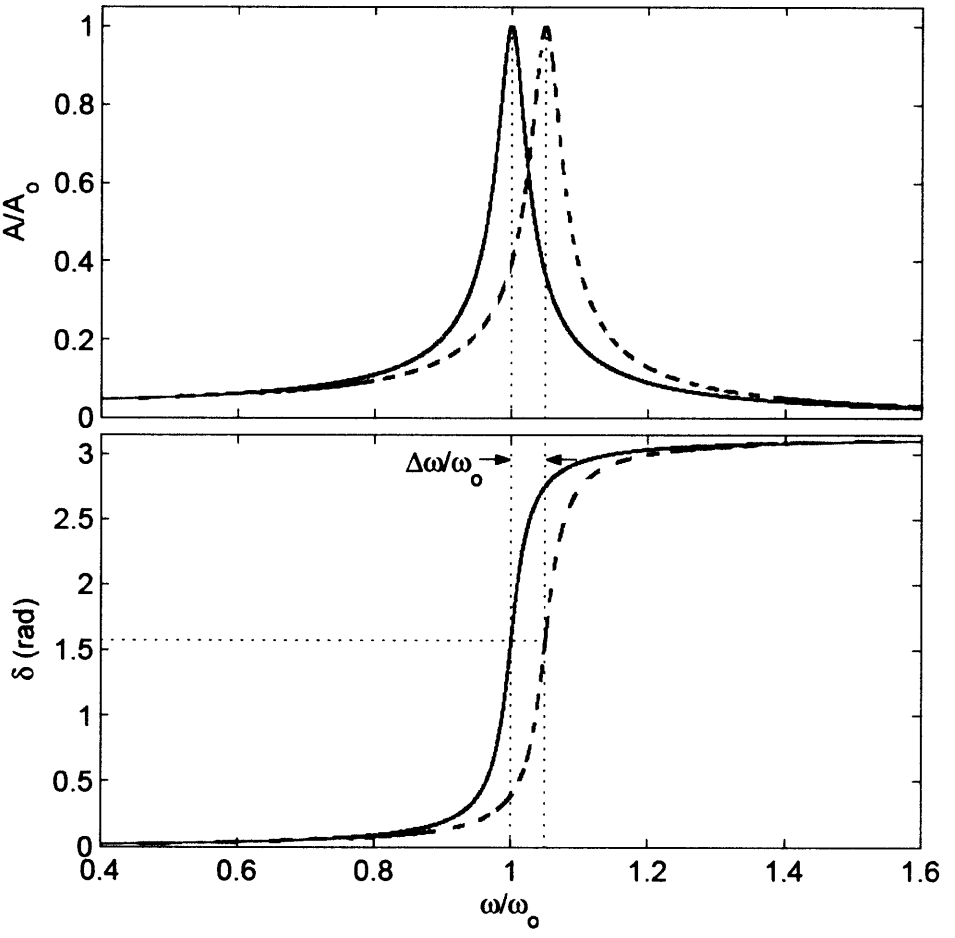

Figure 14: A plot of A and δ as a function of frequency ω. ω_0 represents the resonant frequency of the cantilever. The red dashed and blue solid curves represent two different force gradients, which result in two different excitation frequencies. In FM detection, the phase shift changes to maintain a constant value of $\pi/2$ to keep the cantilever on resonance as it moves through a force gradient. Figure from [1].

4 Instrumentation and Experiment Setup

The magnetic force microscope used for this thesis was constructed by Eric Straver of Stanford University, and is based on a design by Dan Rugar, of IBM Almaden, for his magnetic resonance force microscope [23]. In this section, I will highlight the features and components of the device. For further discussion of the details of the MFM design see reference [1].

4.1 Instrument Design

The MFM is a delicate instrument that combines many different aspects of engineering and physics to work correctly. This MFM implements a microfabricated cantilever in a variable low temperature environment in high vacuum under several layers of vibration isolation, using homemade electronics and control software and a laser interferometer setup to make measurements. I discovered two things during the course of my summer research on this device. First, getting these independent systems to work together and behave such that measurement possible is no simple task, as each problem that arises could be the result of several sources of error. Second, once working, the MFM is a powerful tool that allows several different kinds of measurement in a wide scope of environments, making its built in versatility well worth the effort.

4.2 Vibration Isolation

There are three levels of vibration isolation on this MFM. First, air legs act to minimize vibrations on the optical table due to the ground. Second, a set of three bellows isolates the probe from the table (figure 15). Finally, a set of teflon springs damp any vibrations that travel down the probes attachment rods towards the microscope head (figure 17). No vibrations show up in measurements, so vibrations are not the limiting factor in measurement resolution or signal to noise calculations. On this probe, in order to change the tip or sample, or make adjustments to the probe head, the probe must be removed from the table/dewar setup. It is easy to destroy a day's work aligning the tip with the sample during the process of returning the probe to the dewar for cooldown.

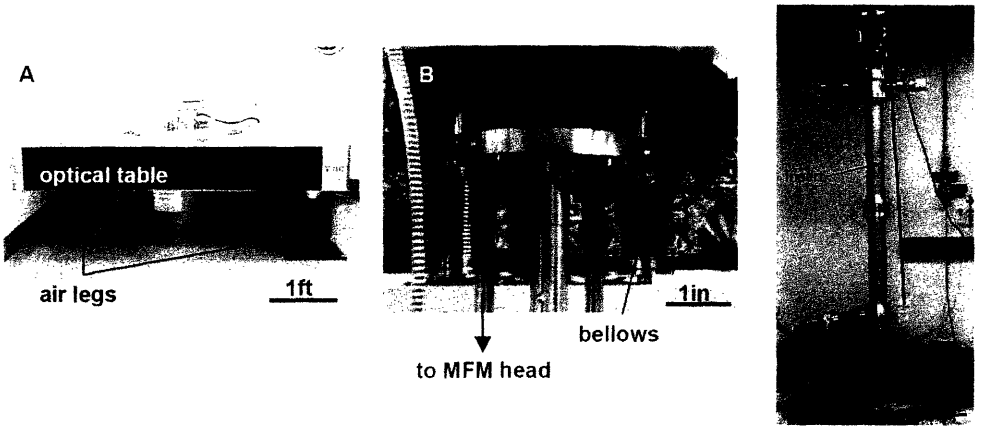

Figure 15: This figure shows two main aspects of the vibration isolation system, in (A) the optical table and pressurized air legs, in (B) the bellows from which the probe hangs. (A) also shows the dewar containing a 5 Tesla magnet. (C) shows the removable probe insert. This figure was taken from [1].

4.3 Vacuum System

The vacuum system on the MFM consists of a Pfeiffer TMU 071 turbopump, a Varian SH-100 dry scroll backing pump, and a Pfeiffer Full-Range Gauge. The turbo and backing pump combine to bring down the pressure to the 10^{-7} to 10^{-8} Torr regime. For all permanent connections on the probe, inserts are vacuum sealed using conflat flanges with copper gaskets. The probe head part of the insert is vacuum sealed by the use of an indium O-ring. Since the turbo pump is mounted to the table, it is connected to the insert via a KF flange-gate valve setup (shown in figure 16). The gate valve allows the turbo pump to be turned off during experimentation to lower vibrations, since at operating temperatures cryopumping is more effective than the turbopump. There is also a smaller gate valve for the use of a venting line. Venting with nitrogen while the microscope is unsealed prevents some water from condensing on the inside of the microscope. This shortens pumpdown times considerably.

4.4 Cryogenics

The dewar used in this MFM is a liquid helium dewar by Precision Cryogenics, and contains a 5 Tesla superconducting magnet. Considerations were taken in dewar design to reduce helium boil off rate, increasing the time a given set of experiments can run for (about 5 to 7 days depending on magnet usage [1]). The length of the

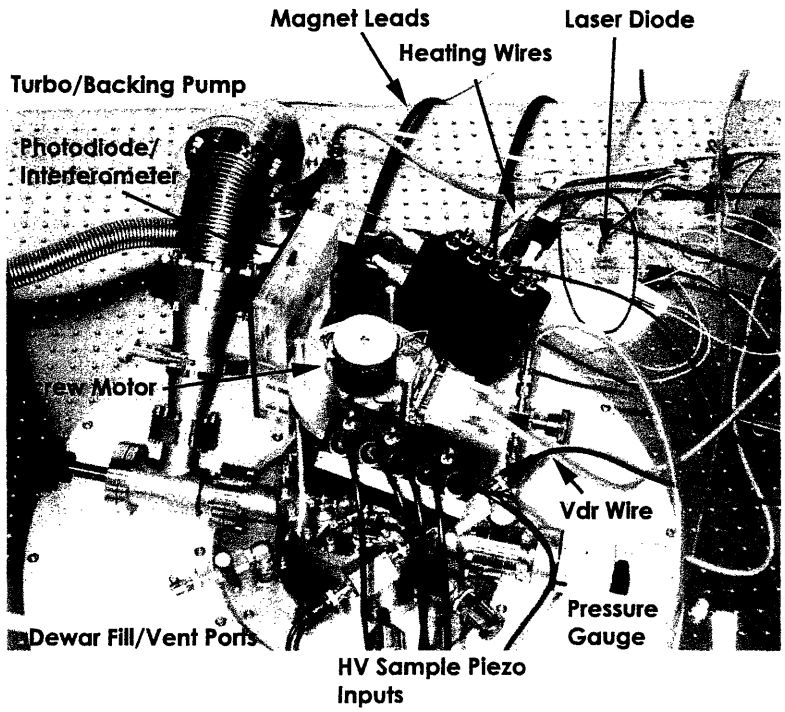

Figure 16: The top of the probe as connected during experimentation. Picture taken by Jenny Hoffman.

probe is such that during a run the probe head sits squarely at the center of the magnet.

To control and monitor temperature, two Lakeshore Cryogenics Cernox sensors are attached to the probe head. A 25 Watt heating wire is also attached to the probe head via a copper braid from the probe top. One sensor is attached close to the heater wire, while another is mounted directly to the sample holder, as close to the sample as allowable. Together with a Lakeshore temperature controller, using a PID (Proportional gain, Integral gain, Derivative gain) controller, the temperature of the cryogenic bath is controlled. Temperature resolution was $\Delta T = \pm 0.001$ K.

To aid in the cooldown or warmup time, an exchange gas of either helium or nitrogen can be used, however, this has led to problems during operation when bubbles of helium or nitrogen gas get trapped in between the screw threads of the probe head. Given this issue, the gain in warmup/cooldown time is not worth the pain during experimentation, and thus an exchange gas was not used in this experiment.

4.5 Probe Head and Coarse Approach

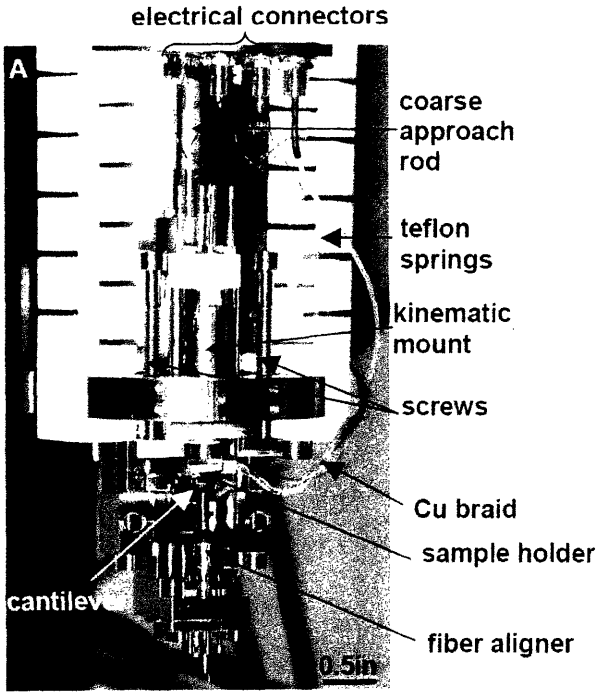

Figure 17: The head of the probe of the MFM. This figure taken from [1].

The head of the probe makes up the bottom section of the insert, figure (17). Each time the tip or sample is changed, the bottom cover of the insert is removed and the probe head is exposed. With a few exceptions, all of the metal on the probe head is either titanium or copper. Titanium is preferred to stainless steel in order to minimize random magnetic signal due to materials in the device. The probe uses several different types of connectors wires in order to measure temperature, apply high voltages to the piezos, and apply driving voltages to the sample.

The coarse approach mechanism is a crucial element to MFM, and perhaps the hardest to design. This microscope was designed before the widescale availability of piezo-based course motion devices, such as those sold by Attocube Systems AG, and in the future a better implementation for coarse approach would use such a device. This MFM uses a 1/4-80 fine pitch screw attached through a rotary feedthrough to a stepping motor. The stepping motor allows for half-degree increment rotation control of the screw. The turning screw then moves the kinematic mount forward

or backward. A half degree turn of the screw corresponds to approximately .25 μm of motion between the tip and sample. Often, the screw will fail to turn in small increments, instead jerking every several steps due to the friction between the screw and its mount. This has the been the reason behind many failed runs due to crashed cantilevers and destroyed samples. To minimize friction, MoS_2 dry lubricant is used. Attempts to use a differential screw to reduce friction due to the fine thread pitch of the existing screw were unsuccessful because the differential screw was too loose to provide precise position control.

4.6 Piezo Fine Motion Control

A piezoactuator (piezo) is a ceramic material that changes shape under external forces, via applied stress or under applied electric field. Piezos are commercially sold to extend or contract in a specific direction under an applied voltage. The spatial extent of this effect is small, and is related to the inter-atom electric fields present in a crystal lattice. This makes it ideal for fine motion control. Piezo motion is a temperature dependent effect, which means that at operating temperatures (typically beneath 100 K), we need to apply significantly more voltage to a piezo to get the same amount of displacement as we would get at room temperature. As a result, each piezo used in this device has an associated high voltage amplifier to drive the piezo motion.

There are two distinct piezos used in this MFM. During operation, the cantilever piezo maintains a constant voltage set in order to obtain maximum resolution from the interferometer. Before each run, this operating point is calibrated and set. The sample piezo, made by Staveley Senors, has four silver outer electrodes and a single inner electrode. The piezotube itself is mounted on a kinematic mount in order to control the angle between the tip and sample. The sample piezo is the one that controls scanning motion. To obtain images, the cantilever is held fixed in place, and the sample is moved. Due to tip/sample angle and the slightly parabolic motion of the sample, before each run the sample piezo is calibrated with a set of five coefficients to account for both sample slope and sample motion. Typically, the slope of the sample dominates over quadratic sample motion effects. A cartoon illustrating the motion of a five-quadrant piezo is shown in figure (18).

One common problem for high resolution imaging via piezo scanning is the presence of piezo creep. Piezo creep is a relaxation effect whereby a piezo that has been constantly scanning a given distance back and forth will be "warmed up" such that it will scan a desired input distance to greater accuracy than a piezo that has been

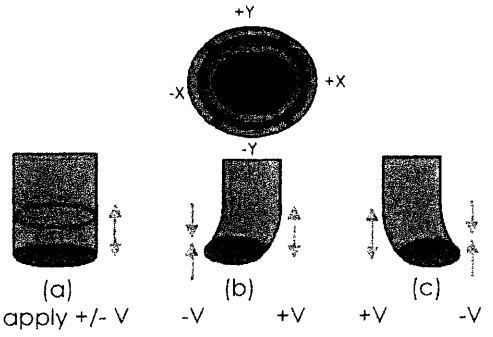

Figure 18: A cartoon illustrating the control of a five-electrode piezo. Z motion is achieved by applying a voltage to all electrodes. X-Y motion is achieved by applying opposite voltages to the plus and minus electrodes in the desired direction.

at rest for some time and is suddenly called into action. This problem is very hard to characterize as it is different for every piezo at every temperature. To work around this, all imaging done in this thesis was "prescanned" before any image was taken. Thus a given area was scanned at the desired height several times very quickly before the actual image was taken, at higher resolution and slower speed.

4.7 Interferometer

This MFM uses a fiber optic interferometer coupled with a photodiode sensor as a deflection sensor. Since laser heating has been known to affect silicon cantilever frequency, a 1310 nm laser was chosen because it is above the bandgap of Si and thus minimizes laser absorption [1]. A PD-LD, Inc. InGaAsP Fabry-Perot laser diode with wavelength equal to 1310 nm was used. The laser input attaches to a dual stage optical isolator, which attenuates both the input and output signal of the fiber optic, further preventing cantilever heating and preventing laser feedback into the photodiode. The interferometer setup is illustrated in figure (19). The reflection off of the end of the fiber interferes with the reflection off the cantilever, constructively or destructively based on the optical path length difference between the two reflections.

The cantilever is mounted on its own piezo in order to adjust the optical path length such that the interferometer operates in a regime of high sensitivity. During alignment, the cantilever piezo is swept through all accessible voltages (limited by the breakdown voltage of the piezo) to determine this point of maximum sensitivity. There is a sinusoidal dependence on optical path length d, as you pass through

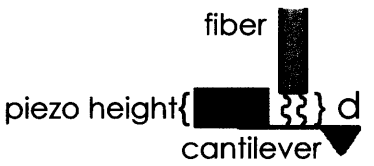

Figure 19: Rather than use a mirror, deflection is measured by the optical path length difference between internally reflected light and cantilever reflections.

maxima and minima as the two light rays interfere. For maximum sensitivity, the interferometer is operated at the point of maximum slope of this curve,

$$\frac{\Delta d}{\Delta V} = \frac{\lambda}{2\pi(V_{max} - V_{min})}. \tag{14}$$

Experimentally, V_{max} and V_{min} are found by sweeping the cantilever piezo through its entire range (-200 to 1000 V) to find the point of optimal operation where the slope is the largest. The cantilever piezo is then locked at this voltage.

4.8 Noise

Cantilever choice affects the minimum detectable force gradient of the MFM. The main two contributions to noise are interferometer noise and cantilever thermal noise. The minimum detectable force gradient for thermal measurements is given by [21],

$$\frac{dF_{min}}{dz} = \frac{1}{A}\sqrt{\frac{4kk_BTB}{Q\omega_0}} \tag{15}$$

whereas for interferometer limited measurements, the minimum detectable force gradient is [1]

$$\frac{dF_{min}}{dz} = \frac{2kn_{\Delta x}B^{3/2}}{\sqrt{3}\omega_0 A} \tag{16}$$

where $n_{\Delta x}$ is the deflection sensor noise energy density. In both cases, a small spring constant k along with a large resonant frequency ω_0 is desired to maximize sensitivity.

In this setup, resolution is limited by the interferometer sensitivity in all locations except near cantilever resonance. This property of the system is important to operation. The natural resonant frequency of the cantilever can be found by simply looking for a thermal peak in the deflection spectrum. An example of a thermal peak and off-resonance noise is shown in figure (20). This resonance is then locked into

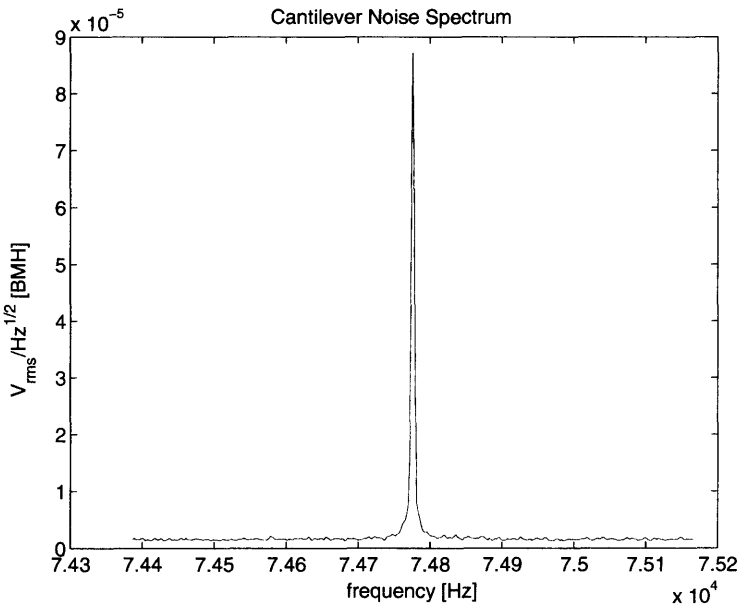

Figure 20: A sample noise spectrum as measured by a spectrum analyzer. Clearly visible is the thermal peak representing the resonant frequency of this cantilever. The baseline on either side of resonance is the interferometer noise contribution.

the electronics to drive at that resonant frequency. A good check of whether your cantilever survived alignment and cool-down is to check for this thermal noise peak.

Off resonance, interferometer noise is a result of laser noise, Johnson noise, and shot noise [1]. The shot noise gives the largest contribution to this noise, such that the signal-to-noise ratio scales like

$$SNR \sim \frac{\Delta P}{\sqrt{P_0}} \tag{17}$$

where ΔP is the change in power into the photodiode, and P_0 is the average laser power incident on the photodiode [1]. While it would make sense to increase laser power, too much power will heat the cantilever, changing it's resonant frequency, or worse it will drive the cantilever, throwing off the FM detection.

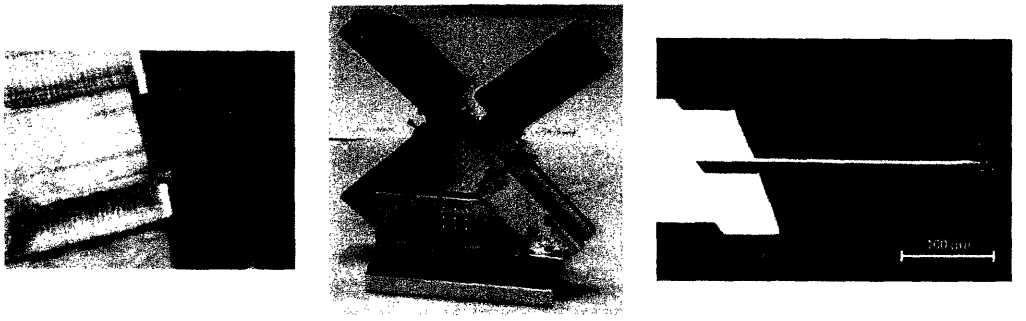

Figure 21: Left to right. A zoomed in picture of a cantilever ready for evaporation. The windmill setup for evaporation jig, where the evaporation direction is vertically down on the jig. An SEM of the type of cantilever used in this experiment, an NSC-18 by Mikromasch. Jig pictures by Jenny Hoffman, SEM image by Mikromasch.

5 Data and Scan Method

This section outlines the preparation of the experiment, starting from the creation of a magnetic-tipped cantilever, and ending with some sample images of the surface.

5.1 Scan Details

First, the desired tip must be coated with magnetic material. Note that the thickness given for the various coatings is for a surface perpendicular to the direction of evaporation. Since the alignment jig for shadow masking is oriented in the plane of the cantilever, we avoid covering the entire cantilever with magnetic material, limiting the addition of magnetic material to the tip. This process of evaporation is by no means perfect. Though it is expected to have one side of the tip coated, kinetic energy of deposited materials will most likely cause some coating to occur on the opposite side of the tip. Furthermore, since the tip is not a perpendicular surface to the evaporation direction, not all of the 60 nm of magnetic material will land on the tip. In reality, the amount is probably less.

In our tip modelling, we have accounted for both of these effects, and have provided two different models for the total magnetic moment of the tip. In one model, it is assumed that the tip is evenly coated on all sides by 16.5 nm of Fe. In another model, it is assumed that the tip was ideally coated by 33 nm of magnetic material on only one side. Once the cantilever has the magnetic material evaporated onto it, a rare earth magnet (NdFeB) was brought close to the tip to magnetize the magnetic

material in one direction.

An ideal magnetic tip would be a magnetic monopole at the end of the tip of the cantilever. Currently, efforts to make cantilevers that better approximate this behavior are being explored using carbon nanotubes at the end of traditional cantilever tips. [34].

The sample used in this experiment is a thin film, 200 nm thick, of optimally doped YBCO grown by pulsed laser deposition [36], with a T_c of 89.8 K [1]. It was grown by Rob Hughes in John Preston's lab at McMaster University. The sample in this experiment is one of four identical samples, another of which was used in [1]. An AFM image of the surface was taken by Rob Hughes, and is included here for reference in figure (22).

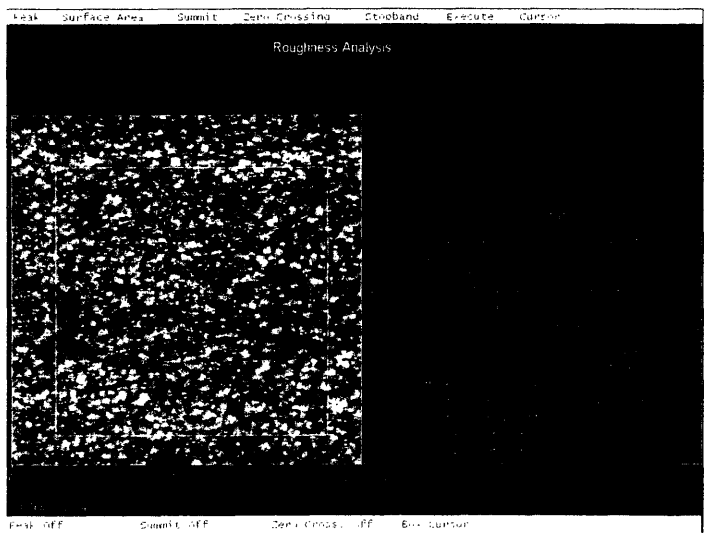

Figure 22: An AFM image of the YBCO sample used this experiment, taken by Rob Hughes of MacMaster University. The rms surface roughness is 5.8 nm. The smoother the surface, the easier it is to obtain an accurate reading of the magnetic topography of the surface.

The tip and sample are then epoxied/glued onto their respective holders and screwed onto the microscope head. The alignment process takes about a day, and involves first aligning the fiber optic wire to the cantilever, and then aligning the cantilever/fiber combination to the sample. Details of how to do this are outlined in [1], though an updated, more detailed version has been created by Jenny Hoffman and myself. Figure (23) shows post-alignment figures of the tip and sample.

Figure 23: Left to right. A picture of the sample, attached via silver paint, to the sample holder, with the cantilever and fiber positioned over the surface. Pictures at two different angles of the tip much closer to the sample.

The sample stage contains the tip and sample, as well as a silver paint glue that holds the sample and the capacitative coupling wire. The silver paint extends onto the sample to provide electrical conductivity to the wire that couples the tip and sample, in order to drive the cantilever on resonance.

During alignment, the distance between the sample is determined by measuring the distance between the tip and its reflection in the surface. When this distance is about two times the width of the cantilever, alignment is finished.

Following alignment, the vacuum can is sealed, and the probe is returned to the table/dewar. Following both pumpdown and cooldown we check the thermal peak to verify that the cantilever is still there (it can and has been destroyed while putting the probe in the dewar). Next we make fringe measurements to determine what voltage to the cantilever piezo gives maximum resolution. At this time the Q of the cantilever is also measured.

Following cooldown, we make a coarse approach towards the surface using the screw. If a measurement at a different temperature is desired, the coarse approach must be used to back up first because thermal contraction of the various components of the device could cause the tip to crash if the tip was within measuring distance of the surface during temperature change.

The coarse approach runs via MATLAB, checking if the cantilever is within the range of the total z-movement of the sample piezo before stepping forward. This allows us to control how close the tip gets to the sample, barring any stick/slip motion of the screw. Close to the sample, the cantilever deflects strongly due to coulomb forces, non-local magnetic forces, and Van der Waal's interactions. By scanning through the range of the z motion of the piezo, the tip sample distance can be derived to within about 10 nm. A sample touchdown curve is shown in figure (24).

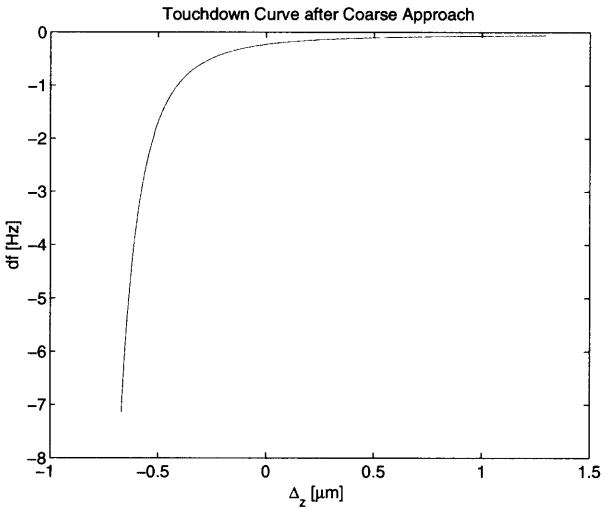

Figure 24: This figure represents the touchdown curve following a coarse approach, where the zero point on the z axis is the point where no voltage is applied to the sample piezo. The rapid force gradient around -.5 [μm] represents the tip strongly interacting with the surface, implying the separation between the two is very small. This is a first order approximation of the tip-sample distance. A negative value is an ideal result for a coarse approach, because if some error during a run causes all high voltages to be shut off, the piezo will return to the zero point, and thus will not crash into the surface.

Once the coarse approach is finished, the tilt of the plane of the sample relative to the cantilever is accounted for. Using a homemade feedback box, a constant-frequency scan [1] is initiated over the entire scanning surface to calculate these plane coefficients. The constant-frequency scan uses a proportional integral controller as feedback into the z portion of the piezo to maintain a constant frequency shift on the cantilever. This, in theory, maintains a constant force between the tip and the sample. While this device works well enough to tell the slope of the sample relative to the cantilever, it doesn't allow for the quantitative force measurements required in this experiment. The constant frequency image used for our data is shown in figure (25).

Following the fit of the plane coefficient, scanning can proceed in search of vortices. The first scan of the sample with this tip is shown in figure (26). To perform measurement scanning, the constant-height scanning program was used [1]. Constant-height scanning works by fixing the height of the tip relative to the sample, and scans in

the x-y direction at that constant height. The computer then records the frequency shift of the cantilever df. Since equation (8) shows a direct relation between force gradient and frequency shift, the raw data images are very useful in showing experimental results, as well as figuring out which scan to take next. To make the depinning measurement, we simply pick a vortex that looks promising and focus on that scan area.

5.2 Scan Method and Data

This section lays out a repeatable measurement process that determines the force exerted vertically downward on a vortex by a magnetic tip via a series of scans at different heights. A set of such scans is then presented.

The MFM is capable of measuring both the force as well as the force gradient. The force gradient was measured using the FM detection method in order to maximize accuracy. In order to extract the force F_z from the force gradient dF_z/dz the force is integrated from height infinity to z_0,

$$F_z = \int_{\infty}^{z_0} \frac{dF_z}{dz} dz \tag{18}$$

where z_0 represents the minimum possible tip-sample distance before the vortex depins. Using the model developed earlier, we can replace the force gradient term of this integral with our measured result from our data, df the frequency shift of the cantilever. Equation (18) becomes

$$F_z = \int_{\infty}^{z_0} -2k\frac{df}{f_0} dz \tag{19}$$

where k is the spring constant of the cantilever, determined experimentally, and f_0 is the resonant frequency of the cantilever, as determined by the thermal noise peak.

The available scanning range limits the number of data points included in this integral. Since coarse motion messes up both positioning and plane slope coefficients, we are effectively limited by the range of the sample piezo in the z direction. Second, knowing exactly where a vortex is located is made difficult by piezo creep issues.

To resolve these issues, the following scanning scheme was used. The tip was scanned in the x-y direction at 66 different heights starting from the maximum tip-sample distance, and stepping steadily closer towards the surface. At each step we did some fast pre-scanning to minimize piezo creep, followed by slower, higher resolution images of the sample surface. The closest scan occurred at 129.4 nm separation

between the tip and the sample. There is a bit of a tradeoff here, as the closer to the sample you get, the more refined the vortex image and the better the data becomes, however you run the risk of crashing the tip into the sample, making future success with the same tip more difficult.

Since depinning probability increases as the tip approaches the surface, starting high and scanning closer with successive scans allows determination of the depinning force by calculating the force on the vortex on all scans except the one where the vortex moves. An interesting question for future experiments would be to determine if the fluctuation in depinning forces was larger or smaller than the distance between scan height steps.

The number of scan heights is arbitrary. While stepping in smaller height increments is certainly favorable, the time required for such a run yields little extra benefit experimentally. The real limiting factor in this experiment is the upper limit on the tip-sample separation. The farther away this experiment is started, the more accurate the force integral becomes. This is especially important with regard to our actual numerical result, as our complicated tip geometry makes it difficult to extract out to infinity what the interaction looks like. The bounds on our numerical result for the depinning force are due in large part to estimations on the tip geometry. In future experiments, more idealized tip structures could make such data extraction simple, rendering large tip-sample distance less crucial.

The raw results of an experiment are shown in figure (27). As expected, the vortex image becomes more clear as the tip approaches the sample. There is some evidence of another vortex in the upper left corner of the image. The vortex moved on last scan of the data set, in the forward direction. It was lucky, in fact, to see the vortex move, as it occurred during a data-taking scan, and could easily occurred during one of the unrecorded prescans. The before and after scans of the vortex moving are shown in figure (28). This reinforces the idea that depinning is a thermally activated event, as there were several prescans at the same height but the vortex only moved in one of them. It also suggests that in the future all prescans should be recorded at the same resolution as an actual scans, in the event of depinning while prescanning.

Given this data set, the laboratory work is now done. Calculation of the force from the force gradient, however, is not so straightforward. While the data set contains the force gradient at a number of different heights, to calculate the total force exerted on the vortex requires more information. It is necessary to extrapolate what the force would have been, had scanning occurred at every point in between measurements,

as well as what would have been measured, if the experiment had the capability to extend the integration out to infinite tip sample distance. This post-processing of the data requires modelling in order to obtain a meaningful result.

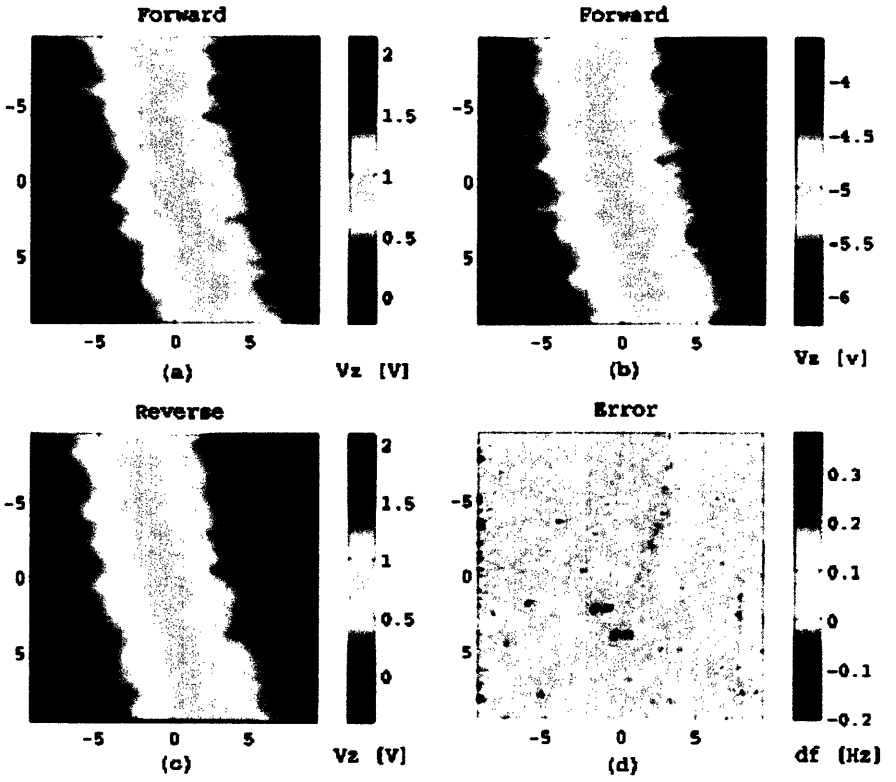

Figure 25: Figures (a) and (c) represent the forward and reverse scans used in the calculation of the plane coefficients via constant frequency imaging. There is some hysteresis from forward to reverse scanning, which is taken into account in calculating the coefficients. Figure (b) and (d) are the forward scan and its error signal respectively for slightly different settings of the PI controller. Notice the increased prominence of the vortices, as well as the "pair" error signals that correspond to the feedback controller trying to compensate as the cantilever passes over a vortex.

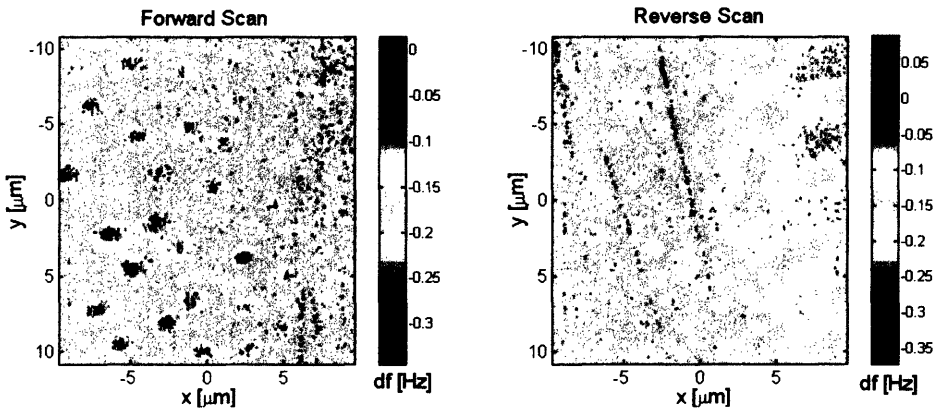

Figure 26: First scan of the sample using a new tip. Clearly visible are individual vortices in a random arrangement, made visible by the magnetic flux passing through them, which is detected by the magnetic tip. Note that this scan was taken with no applied field, so the vortices seen are a result of Earth's magnetic field (.3 Gauss). Also visible are streaks believed to be due to sample reflection of laser light, which distort the interferometer measurement. They are clearly not surface effects as they are not consistent in their strength or location for multiple scans in the same area.

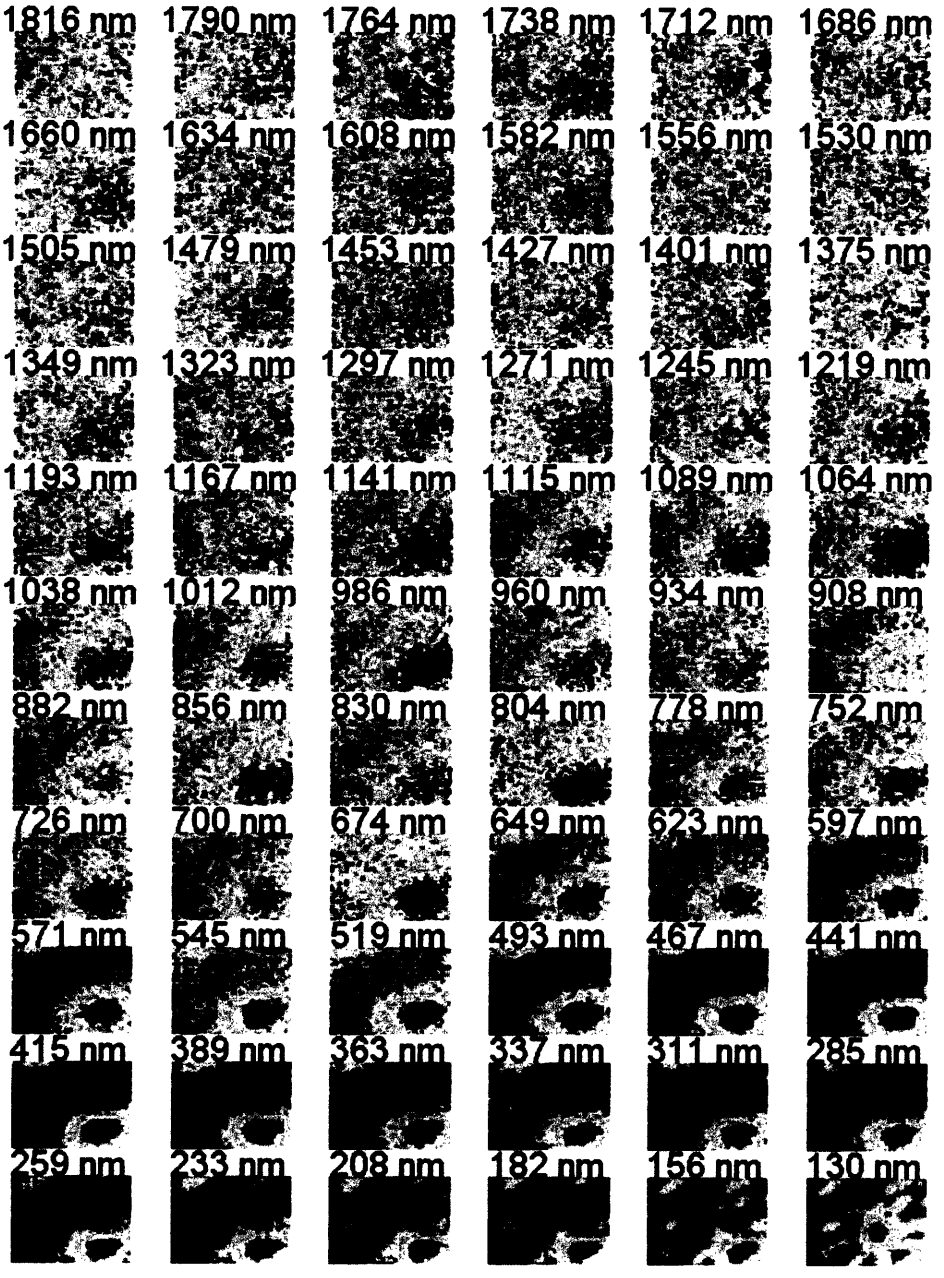

Figure 27: Vortex depinning dataset. Note that in each figure, the x and y scan distance is the same, a total distance of 4.12 μm in the x direction, and 3.39 μm in the y direction (Not shown for clarity). Also note that the color scale is not correlated between figures, such that the color "red" in one sub-figure does not correspond to the same frequency shift as the color "red" in another sub-figure.

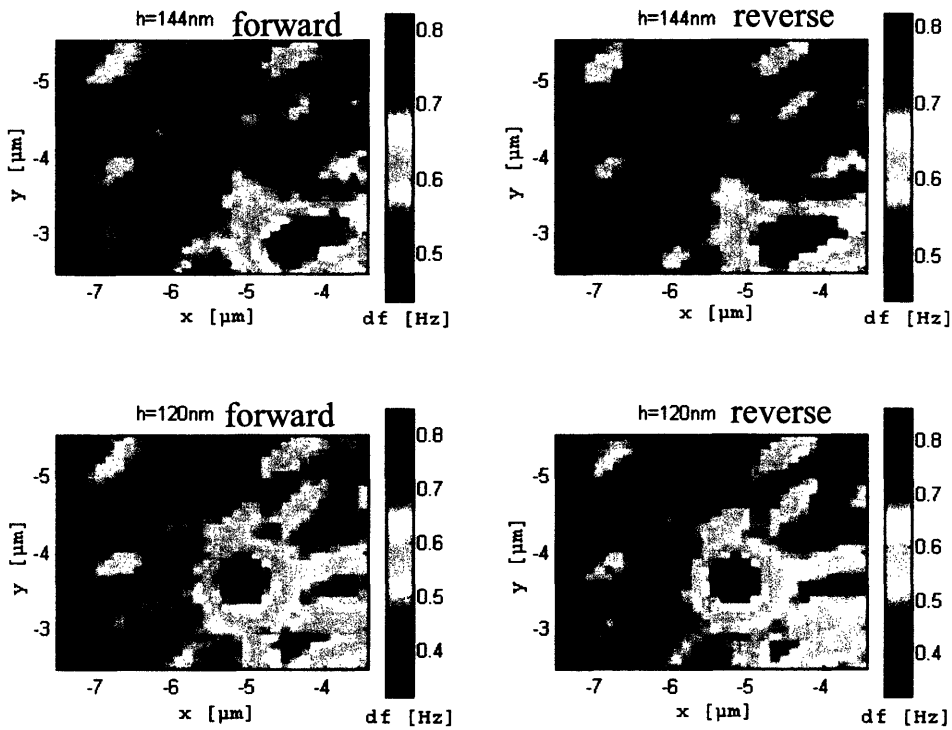

Figure 28: A set of before and after shots of the vortex depinning event. This scan started from the bottom and moved up. The movement occurred between forward and reverse scan lines.

6 Modelling and Results

There are several reasons motivating the need for models to interpret the data and provide an accurate result. By modelling the entire tip-sample interaction, background effects can be subtracted off, tip position and size effects can be accounted for, and extra data points can be extrapolated, which allows for the determination of the most accurate force reading.

6.1 Background Effects

When the tip is moved close to the sample, there are several factors contributing to the total force. Equation 19 is rewritten as a sum of constituent forces to obtain:

$$\frac{df}{f_0} = -\frac{1}{2k}\frac{dF_z}{dz} \tag{20}$$

$$= -\frac{1}{2k}\left(\frac{dF_{vortex}}{dz} + \frac{dF_{Meis}}{dz} + \frac{dF_{ES}}{dz} + \frac{dF_{VdW}}{dz}\right) + \frac{f_{offset}}{f_0} \tag{21}$$

where F_{vortex} is the force under study, F_{Meis} is the force due to the Meissner effect (which is expected to be small because most of the magnetic flux penetrates through vortices, rather than being screened by this effect), F_{ES} is the electrostatic interaction, and F_{VdW} is the Van der Waal's interaction. The term f_{offset} is included to also account for any uniform deviation from the resonant frequency present in a scan. With the exception of the $\frac{dF_{vortex}}{dz}$, the rest of the terms of the equation are relatively constant regardless of where on the material scan the scan occurs. They might be affected by topography, but the sample is clean and smooth enough to bunch these all together as a single background effect.

6.2 Tip Effects

Accurate determination of the force requires calibration of the tip. The force integral used in equation (18) integrates force as a function of distance. Remember that the zero-point for tip-sample distance is determined via a touch down method shown in figure (24). When the frequency shift changes rapidly, it is ascertained that the end of the physical tip is very close to the sample, to within a few nanometers. Since there is magnetic material all over the physical tip, and not only at the end of the tip, there is a separation between the end of the physical tip and the "center of gravity" of the total magnetic moment of the tip. Since this is a magnetic measurement, and

the important distance is between the magnetic material and the sample, a way needs to be found to calibrate between the end of the physical tip and the center of the magnetic material. This yet-to-be-determined calibration distance is called d_{offset}.

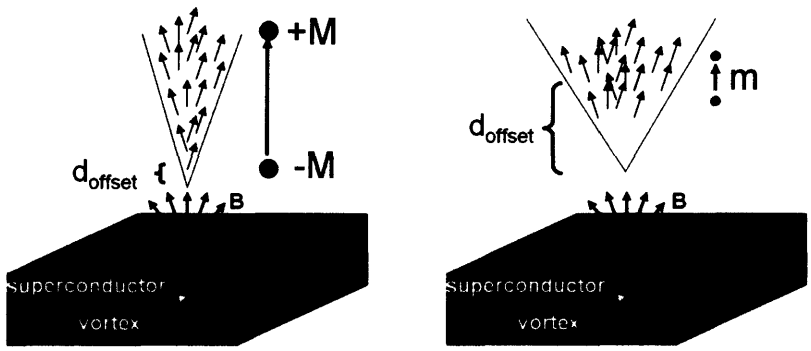

Figure 29: Two cartoons showing the two extremes of tip magnetic behavior. On the left, the individual magnetic moments of the deposited iron add up such that the surface only sees a large monopole-like effect. On the right, there is little material coating the end of the tip, so the sample sees a dipole-like effect. The sample probably sees something in between.

In reality, the tip's magnetic signal is some complicated geometry, that causes a complicated interaction with the sample. It is reasonable, however, to approximate the tip as being somewhere between a pure monopole and pure dipole (see figure (29)). Whether the tip behaves as one or the other has a large impact on the resulting force for the depinning measurement. To accurately extract the force in between the data points our data set, a functional form needs to be found for the force fall off as a function of distance. These two extremes have force fall off relations of $F_z \propto 1/z^2$ for a monopole tip, and $F_z \propto 1/z^3$ for a dipole tip. By modelling the tip as each of these two different interactions, a lower and upper bound can be established for the total force to depin a vortex.

There is one further complication. Through the entire scan, the end of the physical tip moved from being 1.8 μm away to being 0.1 μm away. The entire length of the tip of the cantilever, the good majority of which is covered with magnetic material, is 17.5 ± 2.5 μm. That means that the spatial extent of the tip is large compared to the tip sample distance. This means that at 0.1 μm away, the effective magnetic charge seen by the sample is different than at 1.8 μm away. At the closest point, much of the magnetic material at the far end of the tip is effectively "screened" because the

magnetism at the end of the tip dominates the interaction. As the tip moves away, this "screening" effect decreases, and if the tip were retracted to infinity, the length of the tip would become insignificant, and all the sample would see is a dipole with net magnetic moment equal to the sum of all the spins of the deposited iron. Thus as the scan progresses, the tip actually looks different to the sample. At small distances, the tip to look like a monopole, and at large distances, the tip looks more like a dipole. A cartoon illustrates this in figure (30).

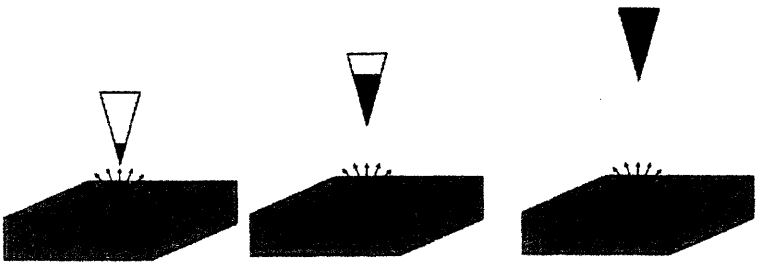

Figure 30: Three cartoons showing how the sample effectively "sees" a different amount of magnetic material depending upon how far away the tip is.

This means that whatever fit to the data is made for d_{offset} should change at every single height, making it very difficult to correctly calibrate the distance axis of the force-distance curve. Thus, rather than quoting a single value for the force as a function of distance, this calculation shows an upper bound and lower bound for the force representing the extremes of the expected behavior: The upper bound force represents a purely monopole tip assumption, and the lower bound force represents a purely dipole tip.

6.3 Vortex Model and Fit

In order to completely model the tip-vortex interaction, a model for the vortex is also needed. In 1966, Judea Pearl [19] proposed two simple models for a superconducting vortex, one of which describes a superconductor well under the surface, and the other near the superconductor's surface. Since we are studying the surface of the material, we will use the latter of the two models. Assuming that the superconductor is essentially an infinite flat plane in the x-y directions, he used the Ginzburg-Landau equations to derive an expression for the surface current density observed at $r \gg \lambda$

as,

$$\mathbf{J}(\mathbf{r}, z = 0) \cong \frac{\Phi_0}{2\pi\lambda\mu_0}\frac{1}{r^2} \tag{22}$$

The magnetic field of a vortex can thus be approximated as a monopole,

$$\mathbf{B}(\mathbf{r}) \cong \frac{\Phi_0}{2\pi}\frac{\hat{r}}{r^2} \tag{23}$$

$$= \frac{\Phi_0}{2\pi}\frac{x\hat{x} + y\hat{y} + (z+\lambda)\hat{z}}{(x^2+y^2+(z+\lambda)^2)^{3/2}}. \tag{24}$$

This approximation works in the limit of $r \gg \lambda$. It has been approximated that the penetration depth of the sample is approximately 0.2 μm ([26] through [30]). The scanning range varies between 0.1 and 1.8 μm, which unfortunately tests the limits of this approximation (This paper was written before the development of high-T_c materials, when all type II superconductors had smaller penetration depths).

Using a monopole/dipole model for the tip and a monopole model for the vortex, a full expression for the force gradient can be derived. Following [6] and [1], the force between the tip and the sample is,

$$\mathbf{F_{ts}} = \nabla(\mathbf{m} \cdot \mathbf{B}) \tag{25}$$

where $\mathbf{B}$ is the signal from the sample, and $\mathbf{m}$ is the dipole moment of the tip. By assuming that the tip is aligned solely in the $\hat{z}$ direction, the derivative of the above expression can be taken to obtain the form for the force gradient

$$\frac{dF_z}{dz} = m\frac{\partial^2 B_z}{\partial z^2}. \tag{26}$$

Using the monopole model for the tip, the magnetic moment m can be expanded as a volume integral of the iron magnetization over the tip

$$m = \int_{tip} \mathbf{M} dV \tag{27}$$

where $\mathbf{M}$ and V are the magnetization and volume of the tip's magnetic material respectively. Assuming that the tip is a point monopole also oriented in the $\hat{z}$ direction, the force gradient expression becomes

$$\frac{dF_z}{dz} = M\frac{\partial B_z}{\partial z}. \tag{28}$$

Plugging in the monopole model for the vortex we obtain expression for the force gradient for a dipole tip,

$$\frac{dF_z}{dz} = \frac{3m\Phi_0}{2\pi}\frac{(z+\lambda)(-3x^2-3y^2+2(z+\lambda)^2)}{(x^2+y^2+(z+\lambda)^2)^{7/2}}, \tag{29}$$

and for a monopole tip,

$$\frac{dF_z}{dz} = \frac{M\Phi_0}{2\pi}\frac{(-x^2 - y^2 + 2(z+\lambda)^2)}{(x^2 + y^2 + (z+\lambda)^2)^{5/2}}. \tag{30}$$

6.4 Fitting Results

Using equations (29) and (30) fits were performed to the data set in order to determine the calibration distance d_{offset}, subtract off background effects, and to calculate a peak amplitude representing the force gradient due directly to the vortex. The matlab function "fminsearch" using a Nelder-Mead nonlinear minimization was used to fit the data set for each scan height. The results of fits on scans at two different heights are shown in figure (32). Using these fits, the calibration distance d_{offset} and the net magnetic moment of the tip are extracted as a function of scan height. If the tip were an ideal monopole or dipole, the magnetic moment and d_{offset} should remain constant, but clearly this is not the case. Figure (33) shows the results of fitting on these two parameters.

6.5 Ideal Tip Calculations

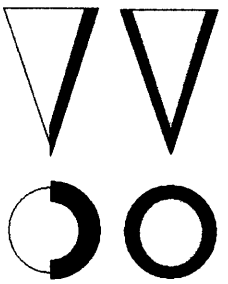

Figure 31: Ideal tip coating structures. On the left, a tip coated only on one side, and on the right a tip entirely covered. Since the total amount of iron must add up to the same amount (60 [nm] on a plane parallel with the height of the cone), the fully covered tip is covered more sparsely than the half covered tip.

The method of fitting used above makes assumptions about how the tip is thought to interact with the sample. However, the method of shadow masking itself is imperfect, and so even this assumption of the tip's magnetic structure is suspect. It is possible, however, to create a false data set of the ideal tip - ideal vortex interaction using the models presented above. By using Mathematica numerical integration techniques and the equations (30) and (31), it is possible to compare the expected results

to the obtained results. This can be used as a check on the modelling techniques used.

If the ideal tip and the theoretical tip are sufficiently similar, then this provides the opportunity to make another interesting measurement using this data. It allows measurement of the local penetration depth λ of the sample, a theoretically interesting quantity that is difficult to calculate.

The shadow masking method used to coat the tip with magnetic material adds about 60 nm of iron to a plane perpendicular to the side face of the tip. The iron being deposited has some velocity when its the tip, so it is likely that some material moves the lee side of the tip. For this ideal tip integration, the integration was performed at two limits of tip coverage. One integration assumes perfect half-coverage of one side of the tip, while the other assumes uniform coverage of the entire tip. This is illustrated in figure (31).

To perform the ideal tip integral, integrate the force gradient contribution from individual volume elements of the tip. This adds up the contribution from individual dipole spins of electrons in the iron to the total force gradient. The saturation magnetization m_{sat} of iron is 1707 Gauss [9]. If $x_0 = 0$ and $y_0 = 0$ represent directly on top of the vortex, the force gradient at a given point is given by,

$$\frac{dF_z}{dz} = \int_{Vol} \frac{3m_{sat}\Phi_0}{2\pi} \frac{(z+\lambda)(-3(x-x_0)^2 - 3(y-y_0)^2 + 2(z+\lambda)^2)}{((x-x_0)^2 + (y-y_0)^2 + (z+\lambda)^2)^{7/2}}, \qquad (31)$$

The newly-created ideal data set, shown in figure (34), is then run through the same fitting routine as the real data set, shown in figure (35). For the purposes of this thesis, included are two types of ideal-data fitting. The ideal data set was taken at the same heights over the same scan area as the real data set, so that the real and fake data are directly comparable.

The results of the close range ideal integrations agree with our logic. The offset term d_{offset} and the magnetic moment of the tip is larger for the dipole than for the monopole as expected (with the exception of small tip-distance). There is also a clear difference between the two types of tip coating.

At close range the real tip looks very little like either type of ideal tip. Furthermore, there is no qualitative difference between the data sets that would allow decision as to which type of ideal tip the real tip best approximates. Thus to extract more information from this data, such as the penetrationd depth λ, would require more knowledge of the magnetic moment and d_{offset} of the tip in addition to what is contained in this data.

6.6 Force-Distance Curves

The calculation of the force-distance curve and depinning force for this vortex is now straightforward. By choosing a reasonable d_{offset} for both the lower and upper bound of the force gradient, the distance axis of the force-distance curve is calibrated. The calibrated force gradient curve is shown in figure (36). The force-distance curve is then found by integrating the force gradient as a function of distance. In order to correctly estimate the force, the force distance curve needs to not only include the data points, but also a correct interpretation of what the falloff should look in between the datapoints, as well as all points outside the range of scanning. Through proper fitting, the force-distance curve is found.

As shown in figure (37), the bounds on the depinning force are between 8-9.5 pN. This can be rougly compared to existing numbers for the critical current taken via bulk measurement. In close to zero magnetic field, the critical current of YBCO ranges from about 200 to 800 Amps [37] [38]. Using equation (1), this corresponds to a force roughly on the order of a few nano-Newton. To correctly correlate the depinning force to the bulk critical current measurement, ideally the same sample would be used in the same conditions to arrive at a result for both the depinning force and the critical current. There are many factors which might be coming into play that might cause deviance between these two force numbers. For example, our sample was in Earth's magnetic field and not zero field. Our sample was a thin film substrate while the samples cited above were created for thick film production and electrical contact industries respectively. Finally our measurement of the force to depin a single vortex is only a single data point in what should be a statistical average of many quoted values. This particular vortex could be a relatively weakly pinned vortex compared to other vortices.

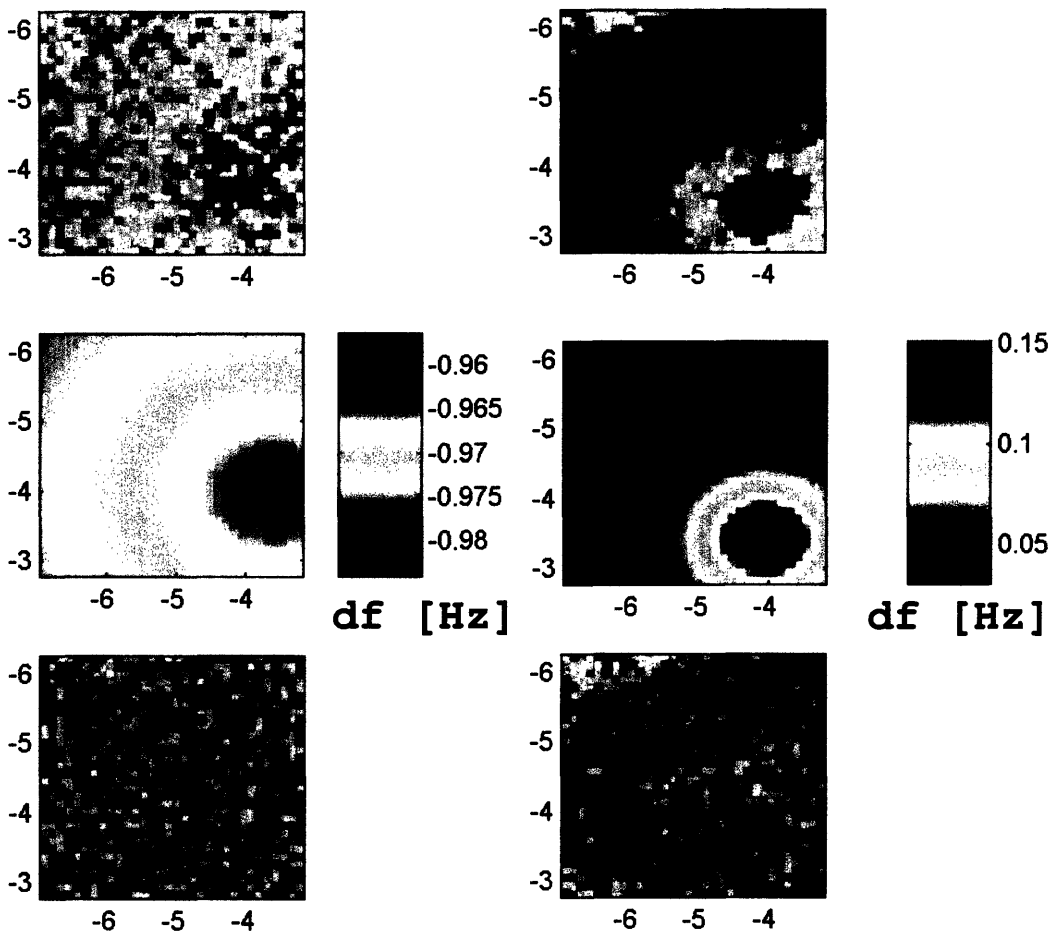

Figure 32: Two examples of fits performed on different scan heights of the data set. Scaling on the x and y axes is in [μm]. The three figures represent, vertically downward from the top, the data, fit, and error respectively. The left figure was taken at a relatively far distance from the sample, and the right figure was taken relatively close to the sample.

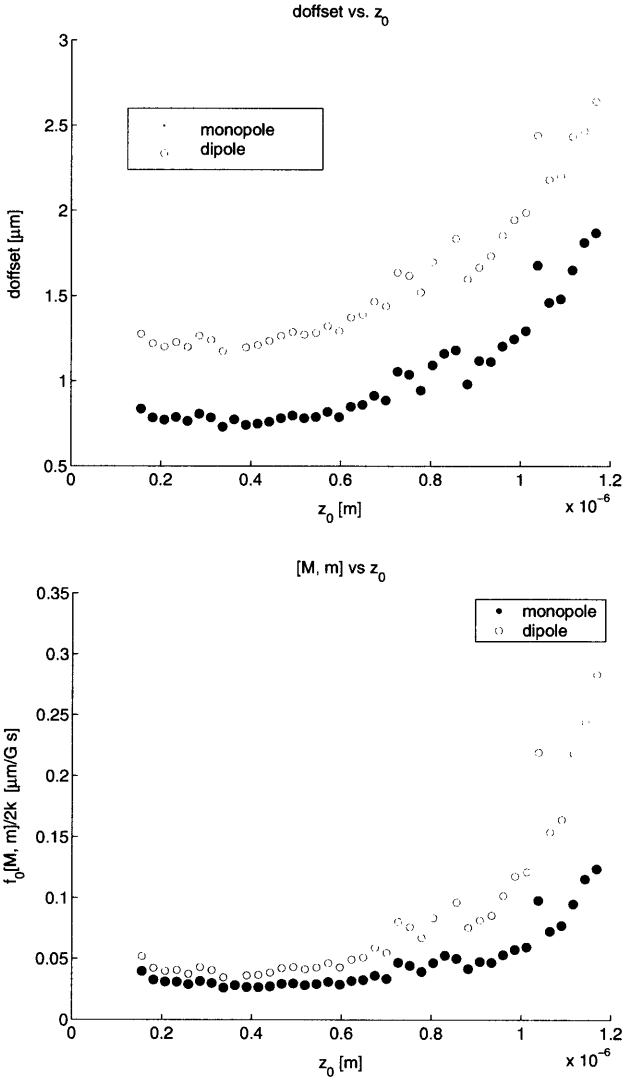

Figure 33: Results of fitting monopole and dipole tip models with a monopole vortex model. The values for d_{offset} show that the tip's magnetic material is at least half a micron away from the end of the tip. This significantly affects the strength of the force-distance curve. The values for the magnetic moment of the tip [M,m] diverge far away from the surface, suggesting that something like the "tip vision" effect described above may be taking place.

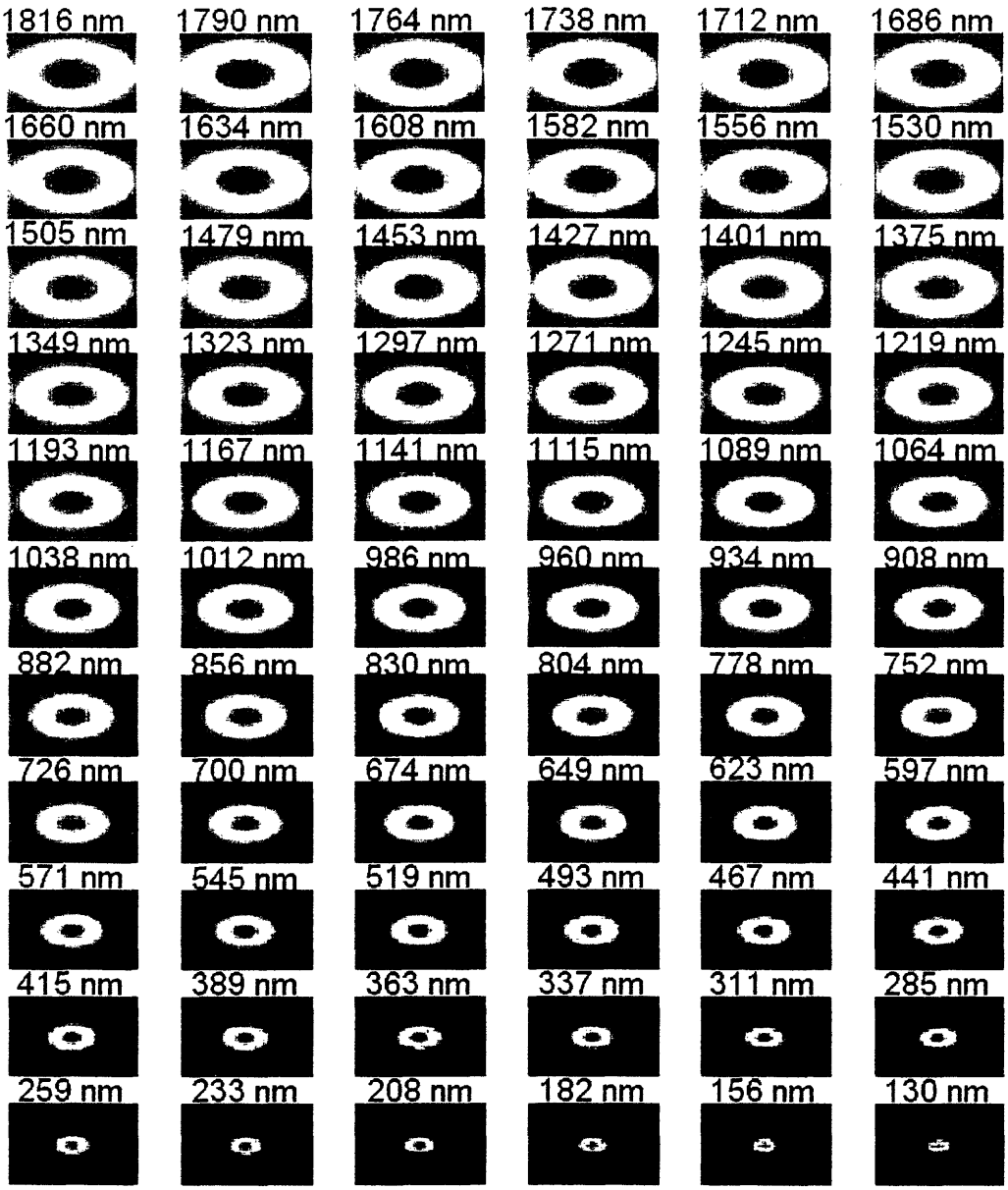

Figure 34: Figure showing the results of an ideal tip - ideal sample integration using the same models as were used to fit the real data. In each case the scan area is the same, but the color scales are uncorrelated, hence red in an upper subfigure does not represent the same force gradient as red in a later subfigure. As expected, as distance from the sample increases, the signal attenuates in magnitude and spreads out uniformly.

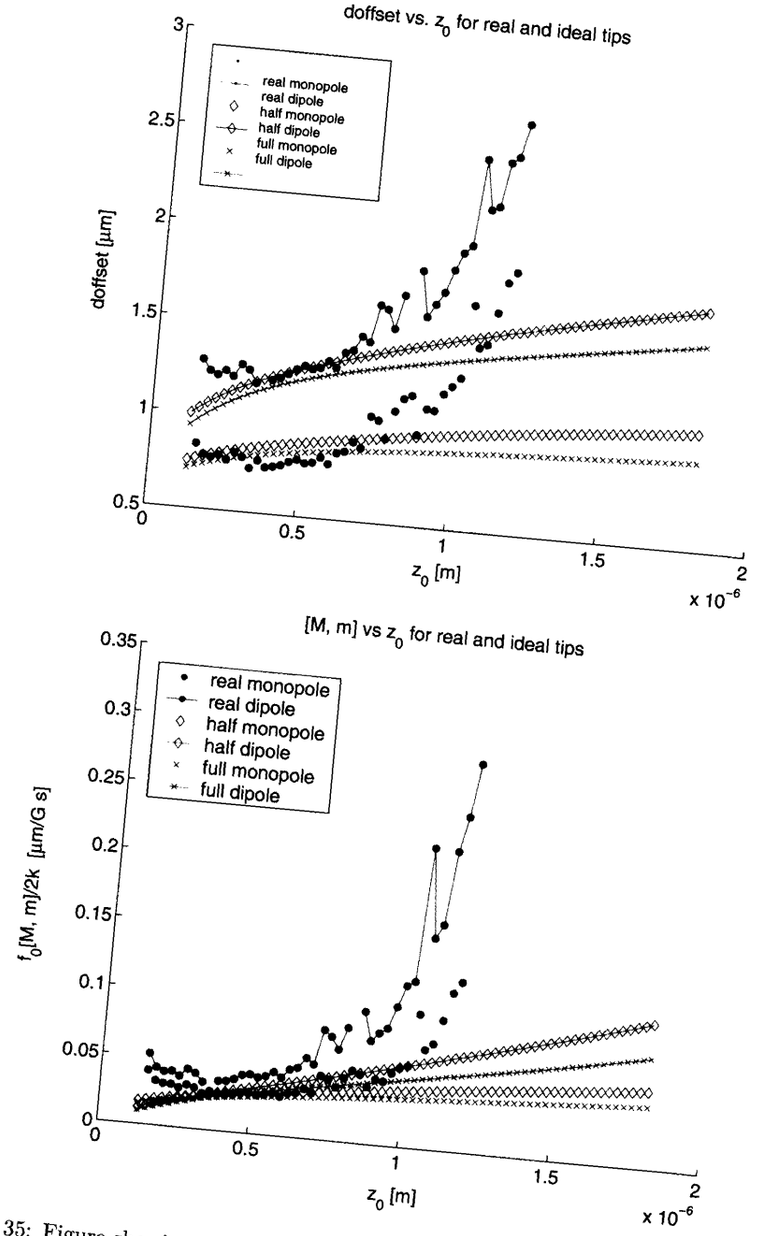

Figure 35: Figure showing the results of fitting the close range ideal data set with the same models as were used for the real data. Real data is overlayed by ideal results, modified for better comparision. In the case of the d_{offset} graph, ideal d_{offset} values are 0.5 higher than actual value. In the case of magnetic moment, ideal values are multiplied by a a factor of ten and then overlayed with real values.

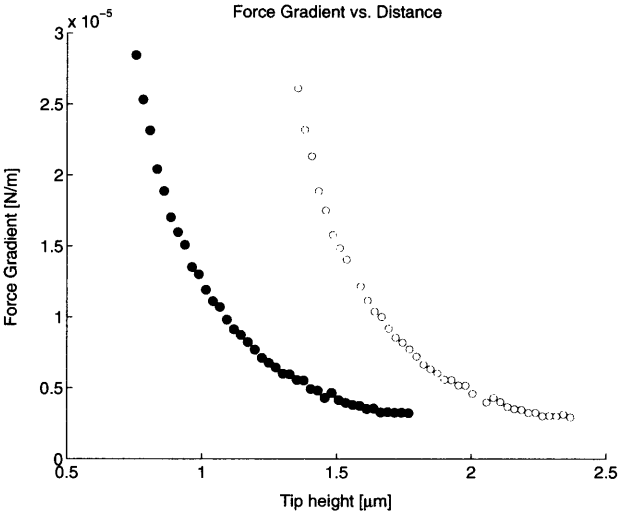

Figure 36: Calibrated force gradient curve for the sample vortex. Notice how the last force gradient measurement is lower than the previous. This is a result of the fitting program unable account for a vortex which depinned partway through the scan.

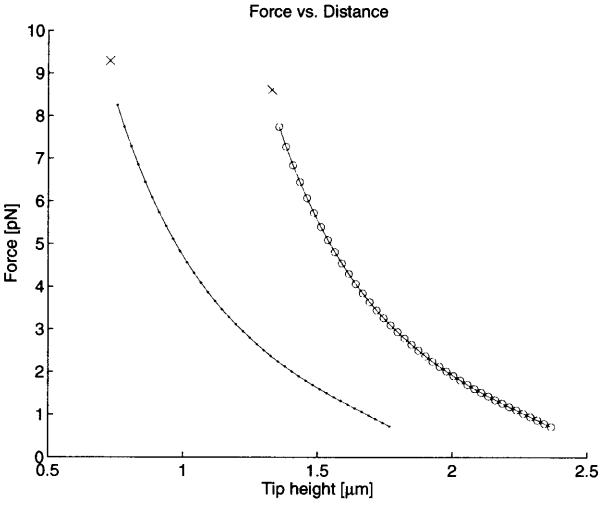

Figure 37: Force distance curve showing lower and upper bounds on force measurement for monopole and dipole tip force-falloff relations.

7 Conclusion

For a single vortex, the depinning force was shown to be between 8 and 9.5 pN. Due to thermal activation of depinning along with inhomogeneous HTSC samples, this number will probably shift and thus represents only a single result in what should ideally be a data driven statistical exercise. This result has profound implication in terms of judging the practicality of various superconducting solutions for new materials, and will certainly help fuel further study.

The data analysis and modelling required focused around the interaction of an unknown tip with an unknown sample. Through reasonable approximation of both, I was able to arrive at a result. However, the limiting factor in this experiment was clearly knowledge of the tip. By either simplifying the tip structure, or more carefully characterizing the tip before the start of an experiment, Not only can the data analysis be made more accurate, but it can simply the work required tremendously.

For this thesis, I have outlined a new process that can be used to study the depinning force of vortices in superconductors. Starting with a working MFM setup, I have shown how a certain set of scan procedures combined with appropriate computer modelling and data fitting can be used to extract a reasonable and important result from a novel, HTSC material. This is the first time a depinning force measurement has been carried out in a HTSC, and the second time (first intentionally) in a superconductor altogether. I have motivated several other current research interests and aspects that have either motivated some aspect of this procedure, or that will help steer future research in the area of this research.

Acknowledgments

There are many people to thank who have supported me and time again throughout my career as a student at MIT. I would first like to thank Henry Abarbanel, who gave me the opportunity to work in his lab as a high school student, and continues to advise me as I grow beyond MIT.

I would like to thank Eric Hudson, for being my strongest supporter at MIT, for advice on all things physics related for, for taking the time to edit this thesis, and especially for connecting me with so many valuable resources which I've tried to take advantage of to the best of my ability.

I would like to thank Kathryn Moler for the opportunity to conduct this research in her lab over this previous summer. This thesis represents just one direction of the many research avenues she pursues, and I wish I could study them all.

Thanks especially go to Jenny Hoffman. I owe her a debt of gratitude for helping me on so many days and nights and weekends, especially when she's supposed to be focused on something due the next day. Over the course of a ten week summer she taught me more about physics than many of my courses put together. Her work ethic, teaching ability, and methods of problem solving are something I have been working to emulate from day one, and I hope it shows in this thesis.

Finally, I would like to thank my parents, Mary Pat and Mark Whitehead. This thesis is dedicated to them. They have continually been there for me whenever I have needed them most. Their wisdom and compassion has shaped me into the person I am today, and I could not be more grateful.

References

[1] E. Straver, *Cantilever Based Measurements on Nanomagnets and Superconductors*, (Graduate Thesis, Stanford University, Aug. 2004).

[2] J. Hoffman, *A Search for Alternative Electronic Order in the High Temperature Superconductor $Bi_2Sr_2CaCu_2O_{8+\delta}$ by Scanning Tunneling Microscopy*, (Graduate Thesis, University of California, Berkeley, 2003).

[3] D. Rugar, *Basic Principles of Atomic Force Microscopy and Magnetic Resonance Force Microscopy*, (Presentation, 2004).

[4] E.W. Hudson *Unpublished.*

[5] J. N. Israelachvili, *Intermolecular and Surface Forces* (Academic Press, San Diego, 1987), page 139.

[6] P. Grütter, H.J. Mamin, and D. Rugar, *Magnetic Force Microscopy* Chapter 5 of *Scanning Tunneling Microscopy II* (Springer Series in Surface Sciences 28, New York, 1992), page 151.

[7] M. Tinkham, *Introduction to Superconductivity 2nd Edition* (Dover, New York, 1996)

[8] J.R. Waldram, *Superconductivity of Metals and Cuprates* (Institute of Physics, Philadelphia, 1996)

[9] C. Kittel, *Introduction to Solid State Physics 7th Edition* (John Wiley and Sons, NJ, 1996) pages 446-449.

[10] G. Bednorz and K.A. Müller, *Possible High T_c Superconductivity in the Ba-La-Cu-O System* (Z. Phys B, **64**, 1986), pages 189-193.

[11] M.K. Wu, *Superconductivity at 93 K in a New Mixed-Phase Y-Ba-Cu-O Compound System at Ambient Presure* (Physical Review Letters, **58**, 1987), page 908.

[12] G. Binnig and C.F. Quate et al, *Atomic Force Microscope* (Surface Science, **181**, (1-2) 1986), pages 145-153.

[13] H.K. Onnes, *Communications from the Physical Laboratory of the University of Leiden* (1911).

[14] W. Meissner and R. Ochsenfeld, *A New Effect Concerning the Onset of Superconductivity* (Naturwissenschaften, **21**, 1933) pages 787-788.

[15] F. and H. London Proceedings of the Royal Society of London (London, **A149**, 71, 1935).

[16] J. Bardeen, L.N. Cooper, and J.R. Schrieffer, *Theory of Superconductivity* (Physical Review, **108**, 1957), pages 1175-1204.

[17] V.L. Ginzburg and L.D. Landau. (Zh. Eksperim. i. Teor. Fiz, **20**, 1950) page 1064.

[18] A. A. Abrikosov, (Zh. Eksperim. i. Teo. Fiz., **32**, 1957), page 1442.

[19] J. Pearl, *Structure of Superconductive Vortices near a Metal-Air Interface*, (Journal of Applied Physics, **37** (11), October 1966), pages 4139 - 4141.

[20] H.F. Hess, et. al, *Scanning-Tunneling-Microscope Observation of the Abrikosov Flux Lattice and the Density of States near and inside a Fluxoid.*, (Physical Review Letters, **62**, January 1989), pages 214-216.

[21] T.R. Albrecht, P. Grütter, D. Horne, and D. Rugar, *Frequency modulation detection using high Q cantilevers for enhanced force microscope sensitivity* (Journal of Applied Physics, **69** (2), 15 January 1991), pages 668-673.

[22] M. Tortonese, *Atomic resolution with an atomic force microscope using piezoresistive detection.*, (Applied Physics Letters, **62** (8), 1993), pages 834-836.

[23] O. Züger, D. Rugar, *First Images from a Magnetic Resonance Force Microscope*, (Applied Physics Letters, **63** (18), 1 November 1993), pages 2496-2498.

[24] M. Roseman, P. Grütter, A. Badía, V. Metlushko, *Flux Lattice Imaging of a Patterned Niobium Thin Film*, (Journal of Applied Physics, **89**(11), 1 June 2001), pages 6787-6789.

[25] J.R. Clem, *Two-Dimensional Vortices in a Stack of Thin Superconducting Films: A Model for High-Temperature Superconducting Multilayers*, (Physical Review B, textbf43 (10), 1 April 1991), pages 7837 - 7846.

[26] C.J. Olsen Reichhardt, M.B. Hastings, *Do Vortices Entangle?*, (Physical Review Letters, **92** (15), 16 April 2004), 157002.

[27] T. Pereg-Barnea, et. al, *Absolute values of the London penetration depth in $YBa_2Cu_3O_{7-x}$ measured by zero field ESR spectroscopy on Gd doped single crystals*, (Physical Review B, **69**, 2004) 184513.

[28] J. E. Sonier, *μSR studies of the vortex state in type-II superconductors*, (Reviews of Modern Physics, **72** (3), July 2000), pages 769-811.

[29] S. Kamal, et. al, *Magnetic Penetration Depth and Surface Resistance in ultrahigh-purity $YBa_2Cu_3O_{7-x}$ crystals*, (Physical Review B, **58** (14), 1 October 1998), R8933-R8936.

[30] J. Lee, T.R. Lemberger, *Penetration Depth $\lambda(T)$ of $YBa_2Cu_3O_{7-x}$ Films Determined from the Kinetic Inductance*, (Applied Physics Letters, **62** (19), 10 May 1993), pages 2419-2421.

[31] J.H. Xu, J.H. Miller Jr., C.S. Ting *Magnetic Levitation Force and Penetration Depth in Type-II Superconductors*, (Physical Review B, **51** (1), 1 January 1995-I), pages 424-434.

[32] J.F. Annett *Unconventional Superconductivity*, (Contemporary Physics, **36** (6), 1995), pages 423-437.

[33] J.R. Kirtley, et. al, *Symmetry of the Order Parameter in the High-Tc Superconductor $YBa_2Cu_3O_{7-x}$*, (Nature, **373**, 19 January 1995), pages 225-228.

[34] Z.F. Deng, K.A. Moler, et. al, *Metal-Coated Carbon Nanotube Tips for Magnetic Force Microscopy.*, (Applied Physics Letters, **85** (25), 20 December 2004), pages 6263-6265.

[35] Mikromasch *NSC18 No Al Datasheet*, (http://www.spmtips.com/nsc18/noal, 10 March 2005).

[36] A.W. McConnell, R. A. Hughes, et. al, *Evaluation of $LaSrGaO_4$ as a substrate for $YBa_2Cu_3O_\delta$*, (Physica C: Superconductivity, **225** (1-2), 10 May 1994), pages 7-12.

[37] K.N.R. Taylor, et. al, *$YBa_2Cu_3O_{7-x}$ thick films on alumina substrates*, (Materials Science and Engineering B, **12** (3), 1 February 1992), pages 237-241.

[38] H. Hirano, et. al, *Properties of a few hundred A class Y-B-Cu-O bulk current leads usable in magnetic fields*, (Physica C, 378-381 (2002), 5 December 2001), pages 827-832.